

Horizontal and vertical propagation and dissipation of gravity waves in the thermosphere from lower atmospheric and thermospheric sources

Sharon L. Vadas¹

Received 11 May 2006; revised 6 January 2007; accepted 29 January 2007; published 8 June 2007.

[1] The dissipation of high-frequency gravity waves (GWs) in the thermosphere is primarily due to kinematic viscosity and thermal diffusivity. Recently, an anelastic GW dispersion relation was derived which includes the damping effects of kinematic viscosity and thermal diffusivity in the thermosphere and which is valid before and during dissipation. Using a ray trace model which incorporates this new dispersion relation, we explore many GW properties that result from this dispersion relation for a wide range of thermospheric temperatures. We calculate the dissipation altitudes, horizontal distances traveled, times taken, and maximum vertical wavelengths prior to dissipation in the thermosphere for a wide range of upward-propagating GWs that originate in the lower atmosphere and at several altitudes in the thermosphere. We show that the vertical wavelengths of dissipating GWs, $\lambda_z(z_{\text{diss}})$, increases exponentially with altitude, although with a smaller slope for $z > 200$ km. We also show how the horizontal wavelength, λ_H , and wave period spectra change with altitude for dissipating GWs. We find that a new dissipation condition can predict our results for $\lambda_z(z_{\text{diss}})$ very well up to altitudes of ~ 500 km. We also find that a GW spectrum excited from convection shifts to increasingly larger λ_z and λ_H with altitude in the thermosphere that are not characteristic of the initial convective scales. Additionally, a lower thermospheric shear shifts this spectrum to even larger λ_z , consistent with observations. Finally, we show that our results agree well with observations.

Citation: Vadas, S. L. (2007), Horizontal and vertical propagation and dissipation of gravity waves in the thermosphere from lower atmospheric and thermospheric sources, *J. Geophys. Res.*, 112, A06305, doi:10.1029/2006JA011845.

1. Introduction

[2] Gravity waves (GWs) have been observed in the thermosphere for many decades as traveling ionospheric disturbances (TIDs) [e.g., *Hocke and Schlegel*, 1996; *Hocke et al.*, 1996; *Oliver et al.*, 1997; *Djuth et al.*, 1997, 2004]. Many of these observed and modeled GWs are from auroral sources in the lower thermosphere at high latitudes [*Hocke and Schlegel*, 1996; *Richmond*, 1978; *Hickey and Cole*, 1988], although medium scale GWs which are thought to arise from lower atmospheric sources have also been detected in the thermosphere with periods less than an hour and phase speeds less than 250 m s^{-1} [*Georges*, 1968; *Waldock and Jones*, 1986; *Crowley et al.*, 1987; *Ogawa et al.*, 1987; *Hocke and Schlegel*, 1996]. GWs from severe storms have been observed as concentric rings in airglow layers near the mesopause, just below the thermosphere [*Taylor and Hapgood*, 1988; *Dewan et al.*, 1998; *Sentman et al.*, 2003]. Reverse ray tracing has shown that the origin of a very large number of medium-scale TIDs (MSTIDs) is

the troposphere [*Waldock and Jones*, 1987]. Additionally, enhanced GW occurrence has been found to occur when convection occurs [*Röttger*, 1977; *Hocke and Tsuda*, 2001], and strong ionospheric activity has resulted from hurricanes and tornados [*Bauer*, 1958; *Hung et al.*, 1978; *Hung and Kuo*, 1978; *Hung and Smith*, 1978; *Bishop et al.*, 2006]. Finally, recent theoretical efforts have shown that GWs from convective sources in the troposphere can propagate well into the thermosphere before dissipating, and the momentum flux divergence which occurs where GWs dissipate in the thermosphere likely results in the excitation of large-scale TIDs (LSTIDs) and MSTIDs and the creation of neutral winds [*Vadas and Fritts*, 2006, hereafter VF2006].

[3] Early theoretical work estimated the effect individual GWs have on the thermosphere [*Hines*, 1960, 1967; *Francis*, 1973]. Until recently, GW propagation in the thermosphere with dissipation was mainly accomplished with multilayer techniques [*Midgley and Liemohn*, 1966; *Volland*, 1969; *Klostermeyer*, 1972; *Hickey and Cole*, 1988], numerical simulations [*Richmond*, 1978; *Francis*, 1973; *Zhang and Yi*, 2002], and approximate or numerical solutions to complex dispersion relations [*Pitteway and Hines*, 1963; *Yeh et al.*, 1975; *Hickey and Cole*, 1987]. Recently, an exact analytic

¹Colorado Research Associates, NorthWest Research Associates, Boulder, Colorado, USA.

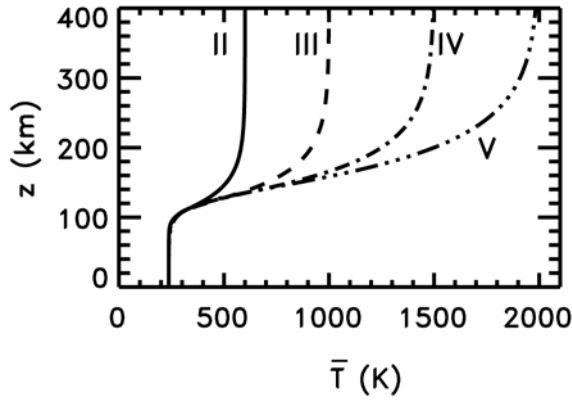


Figure 1. Model temperature profiles II, III, IV, and V as solid, dash, dash-dot, and dash-dot-dot-dot lines, respectively. Temperature profiles II, III, IV, and V have asymptotic temperatures (for example, for $z > 300$ km) of $\bar{T} = 600$ K, 1000 K, 1500 K, and 2000 K, respectively.

anelastic GW dispersion relation was derived which includes kinematic viscosity and thermal conductivity [Vadas and Fritts, 2005, hereafter VF2005]. This dispersion relation is real and was derived from the more general complex dispersion relation by assuming a complex intrinsic frequency and real vertical wave number. This dispersion relation allows for the accurate ray tracing of GWs in the atmosphere when other dissipative mechanism such as ion drag can be neglected.

[4] Although this new dispersion relation has been used to study the thermospheric response to GWs from tropospheric convection [Vadas and Fritts, 2004; VF2006], many GW properties have not yet been explored. The purpose of this paper is to further explore these properties. Our paper is structured as follows. Section 2 contains a brief description of the GW dispersion relation and ray trace model. Section 3 shows GW dissipation altitudes, horizontal distances traveled, and total time taken to dissipate for a wide variety of individual GWs, thermospheric temperatures, and launch altitudes. Section 4 displays vertical wavelength, horizontal wavelength, and intrinsic wave period spectra as a function of altitude for dissipating GWs and compares these results with observational results. Section 5 shows the thermospheric GW spectra that result from a single deep convective plume in the troposphere, with and without a thermospheric shear. Our conclusions are provided in section 6. An Appendix follows.

2. Model Review

[5] Although the average temperature in the lower atmosphere is $\bar{T} \simeq 250$ K, the temperature increases rapidly in the lower thermosphere. During extreme solar minimum, the thermosphere is relatively cold, $\bar{T} \simeq 600$ K. During active solar conditions however, the temperature in the thermosphere can be $\bar{T} \simeq 2000$ K [Banks and Kockarts, 1973]. Figure 1 shows the four canonical temperature profiles we use in this paper. The parameters used to generate these profiles are listed in Table 1 of the work by VF2006, with $\bar{T}_0 = 237$ K. Temperature profiles II and V approximate extreme solar minimum and very active

solar conditions, respectively. From a given temperature profile $\bar{T}(z)$, we determine the pressure, \bar{p} , using the hydrostatic balance equation $d\bar{p}/dz = -g\bar{\rho}$ and the ideal gas law $\bar{p} = R\bar{\rho}\bar{T}$:

$$\bar{p}(z) = p_0 \exp\left(-\int_0^z \frac{g}{R\bar{T}} dz'\right), \quad (1)$$

where $\bar{\rho}$ is the mean density, g is the acceleration due to gravity, $p_0 = \bar{p}(z=0)$, $R = 8314.5/X_{MW} \text{ m}^2 \text{ s}^{-2} \text{ K}^{-1}$, and X_{MW} is the mean molecular weight of the particle in the gas. In addition, $\bar{\rho} = \bar{p}/(R\bar{T})$, the density scale height is $H = -\bar{\rho}(d\bar{\rho}/dz)^{-1}$, the potential temperature is $\bar{\theta} = \bar{T}(p_0/\bar{p})^{R/C_p}$, the buoyancy frequency is $N = \sqrt{(g/\bar{\theta})d\bar{\theta}/dz}$, $C_p = \gamma R/(\gamma - 1)$, and $\gamma = C_p/C_v$. Here C_p and C_v are the mean specific heats at constant pressure and volume, respectively. The density at the ground is set to $\bar{\rho}(z=0) = 1 \times 10^3 \text{ gm m}^{-3}$. This yields densities at $z \sim 125$ km which agree with the thermosphere-ionosphere-mesosphere-electrodynamics general circulation model (TIME-GCM) (see Appendix A). The coefficient of molecular viscosity is

$$\mu = 3.34 \times 10^{-4} \bar{T}^{0.71} \text{ gm m}^{-1} \text{ s}^{-1} \quad (2)$$

[Dalgarno and Smith, 1962]. The kinematic viscosity is $\nu = \mu/\bar{\rho}$ and the thermal diffusivity is $\kappa = \nu/\text{Pr}$. Here we set the Prandtl number to be $\text{Pr} = 0.7$ [Kundu, 1990] and thus ignore its slight variations with temperature [Yeh *et al.*, 1975]. We also set the mean molecular weight and ratio of mean specific heat capacities to be

$$X_{MW} = \frac{1}{2}(X_{MW0} - X_{MW1}) \left(1 - \tanh\left(\frac{s-a}{\Delta_a}\right)\right) + X_{MW1} \quad (3)$$

$$\gamma = \frac{1}{2}(\gamma_0 - \gamma_1) \left(1 - \tanh\left(\frac{s-b}{\Delta_b}\right)\right) + \gamma_1, \quad (4)$$

respectively, where $s = -\ln(\bar{p})$ and \bar{p} has units of gm m^{-3} . Here \ln is the natural logarithm, $X_{MW0} = 28.9$, $X_{MW1} = 16$, $a = 14.9$, $\Delta_a = 4.2$, $\gamma_0 = 1.4$, $\gamma_1 = 1.67$, $b = 15.1$, and $\Delta_b = 4.0$. These parameters represent the best fit for a month of 2004 TIME-GCM data (see Appendix A). The decrease of X_{MW} and increase of γ with altitude represent the change in composition from primarily diatomic N_2 and O_2 to monatomic O. Figure 2a shows X_{MW} and γ using equations (3) and (4). We also show the corresponding altitudes using temperature profile III; in this case, the change from diatomic to monatomic occurs from $z \sim 150$ – 300 km. We also show the local speed of sound, $c_s \equiv \sqrt{\gamma R\bar{T}}$ in Figure 2b. Figure 2c shows the density scale height. Because $H = R\bar{T}/g$ in an isothermal atmosphere and because R increases with altitude, H is twice as large in the thermosphere than if X_{MW} and γ were constant.

[6] Our ray trace model follows the formalism of Lighthill [1978]. The GW dispersion relation we use here includes the primary damping mechanisms for high-frequency GWs with large vertical wavelengths, kinematic viscosity and thermal diffusivity. It is nonhydrostatic and compressible but excludes acoustic waves similar to Marks and Eckermann [1995]. This new anelastic GW dispersion

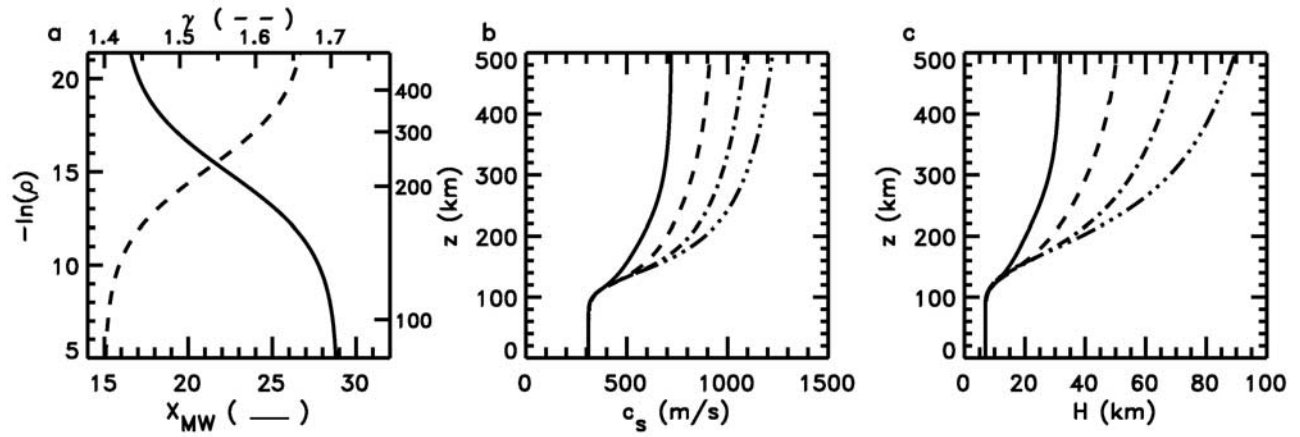


Figure 2. (a) Mean molecular weight (solid line) and ratio of mean specific heats (dash line) as a function of $-\ln(\bar{\rho})$, where $\bar{\rho}$ has units of gm m^{-3} . The corresponding altitudes in a thermosphere with temperature profile III is shown on the right-hand y axis. (b) Sound speed profiles as solid, dash, dash-dot, and dash-dot-dot-dot lines for temperature profiles II, III, IV, and V, respectively. (c) Same as Figure 2b but for the density scale height.

relation can be written as [equation (26) from the work of VF2005, rearranged]

$$m^2 = \frac{k_H^2 N^2}{\omega_{Ir}^2 (1 + \delta_+ + \delta^2 / \text{Pr})} \left[1 + \frac{\nu^2}{4\omega_{Ir}^2} \left(\mathbf{k}^2 - \frac{1}{4H^2} \right)^2 \right. \\ \left. \cdot \frac{(1 - \text{Pr}^{-1})^2}{(1 + \delta_+/2)^2} \right]^{-1} - k_H^2 - \frac{1}{4H^2}, \quad (5)$$

where k , l , and m are the zonal, meridional, and vertical wave number components of the GW, respectively, $k_H^2 = k^2 + l^2$, $\mathbf{k}^2 = k_H^2 + m^2$, ω_{Ir} is the intrinsic frequency of the GW, $\delta = \nu m / H \omega_{Ir}$, $\delta_+ = \delta(1 + \text{Pr}^{-1})$, and $\nu_+ = \nu(1 + \text{Pr}^{-1})$. Note that δ is negative for an upward-propagating GW, because m is negative. This dissipative dispersion relation yields the usual GW anelastic dispersion relation when dissipation is negligible [Gossard and Hooke, 1975]:

$$\omega_{Ir}^2 \simeq \frac{k_H^2 N^2}{m^2 + k_H^2 + 1/4H^2}. \quad (6)$$

Note that the dispersion relation we use here neglects other forms of dissipation such as ion drag and wave-induced diffusion. Ion drag is unimportant during the night for GWs with periods less than a few hours and for GWs with periods less than an hour during the day [Hines and Hooke, 1970; Francis, 1973; Hooke and Schlegel, 1996; Gossard and Hooke, 1975]. Wave-induced diffusion is important for $z \sim 140\text{--}220$ km [Del Genio and Schubert, 1979], whereby it may significantly decrease GW amplitudes with periods longer than an hour or two.

[7] The inverse decay rate in time for a dissipating GW is [equation (25) from the work of VF2005]

$$\omega_{li} = -\frac{\nu}{2} \left(\mathbf{k}^2 - \frac{1}{4H^2} \right) \frac{[1 + (1 + 2\delta) / \text{Pr}]}{(1 + \delta_+/2)}. \quad (7)$$

Therefore a GW's momentum flux (per unit mass) when launched from $z = z_i$ is

$$\overline{u'w'}(z) = \overline{u'w'}(z_i) \frac{\bar{\rho}(z_i)}{\bar{\rho}(z)} \exp(-2|\omega_{li}|t), \quad (8)$$

where we put an absolute value around ω_{li} to ensure that a GW decays in time even when $\mathbf{k}^2 < 1/4H^2$. These expressions, the GW anelastic dispersion relation and decay rate, were derived under the assumption that acoustic waves can be neglected. When dissipation is unimportant, this assumption is $(\omega_{Ir}/c_s)^2 \ll (\mathbf{k}^2 + 1/4H^2)$ [Vadas and Fritts, 2005]. Since a GW propagates at the group velocity, the ray-tracing condition we adopt here is that each GW propagates slower than the speed of sound:

$$c_g \leq 0.9 c_s \quad (9)$$

where the factor 0.9 is arbitrarily chosen. Here $c_g = \sqrt{c_{gx}^2 + c_{gy}^2 + c_{gz}^2}$ is the group velocity in the direction of propagation, and c_{gx} , c_{gy} , and c_{gz} are given by equations (C1), (C2), and (C3) in the work of VF2005. If a GW violates equation (9), it is removed from the spectrum.

[8] In Figure 3, we show the vertical wavelengths, $\lambda_z \equiv 2\pi/|m|$, for GWs launched from $z_i = 0$ (Figure 3a) and $z_i = 120$ km (Figure 3b and 3c) through zero background winds. As a GW propagates upwards in the thermosphere, its raypath bends toward the vertical because its vertical wavelength $\lambda_z \equiv 2\pi/|m|$ increases, with a larger increase when the thermosphere is hot than when it is cold [Richmond, 1978; VF2006]. We also show the dissipation altitudes, z_{diss} , which are the altitudes where each GW's momentum flux (per unit max) is maximum. For GWs launched from $z_i = 0$, λ_z decreases in the lower thermosphere because \bar{T} increases rapidly. Where \bar{T} increases less rapidly (i.e., for $z \gtrsim 120$ km), λ_z increases. If a GW dissipates in a region of the thermosphere where the temperature is approximately constant, its raypath bends rapidly toward

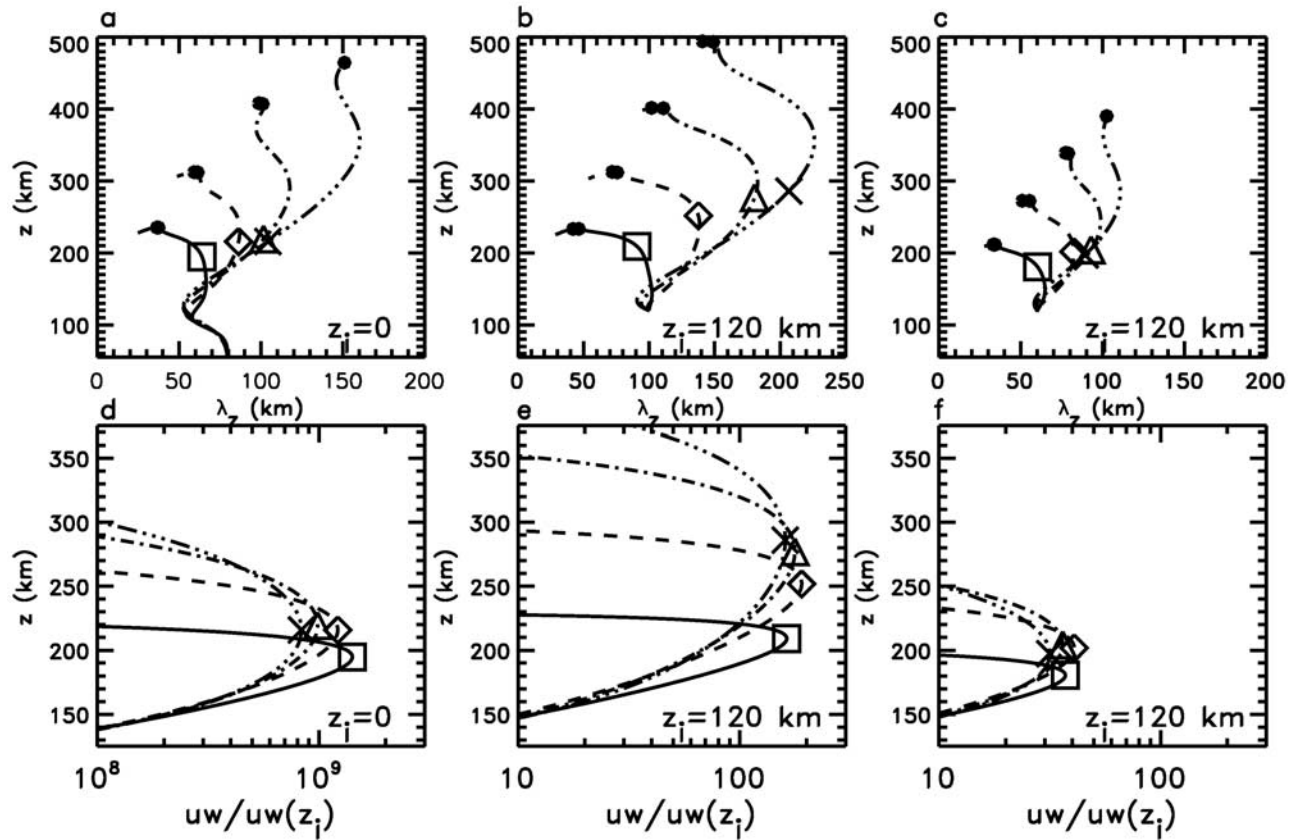


Figure 3. (a) GW vertical wavelengths as a function of altitude. GWs propagate upwards from $z_i = 0$ with $\lambda_H = 160$ km and $\lambda_z(z_i) = 80$ km. The solid, dash, dash-dot, and dash-dot-dot-dot lines are for GWs propagating in temperature profiles II, III, IV, and V, respectively. The squares, diamonds, triangles, and Xs show the altitudes where the GW momentum fluxes (per unit mass) are maximum (i.e., z_{diss}) for profiles II, III, IV, and V, respectively. The solutions between the black circles denotes where $R_2 \geq 1$ using equation (11). (b) Same as in Figure 3a but for GWs which propagate upwards from $z_i = 120$ km and have $\lambda_H = 300$ km and $\lambda_z(z_i) = 100$ km. (c) Same as in Figure 3a but for GWs which propagate upwards from $z_i = 120$ km and have $\lambda_H = 400$ km and $\lambda_z(z_i) = 60$ km. (d) Momentum fluxes (per unit mass) for the GWs shown in Figure 3a with the same linetypes and symbols. (e) Same as in Figure 3d but for the GWs shown in Figure 3b. (f) Same as in Figure 3d but for the GWs shown in Figure 3c. Note that the altitudes displayed in Figures 3d–3f differ from those in Figures 3a–3c.

the horizontal because λ_z decreases rapidly [VF2005; Zhang and Yi, 2002]. However, if a GW instead dissipates in a region of the thermosphere where the temperature increases, its raypath continues to bend toward the vertical because λ_z continues to increase above its dissipation altitude.

[9] A GW's dissipation altitude, z_{diss} , increases as \bar{T} increases. The result that GWs dissipate at higher altitudes during active solar (and day time) conditions than during extreme solar minimum (and nighttime) conditions has been studied previously [Pitteway and Hines, 1963; Francis, 1973; Yeh et al., 1975; Richmond, 1978; Cole and Hickey, 1981; VF2006] and occurs because of the substantial increase of λ_z with \bar{T} . This effect is enhanced for $z > 250$ km, where ν increases less rapidly with altitude for hotter as compared with cooler thermospheres.

[10] In Figure 3d–3f, we show the GW momentum fluxes (per unit mass), $\overline{u'w'}$, for the GWs from Figure 3a–3c, respectively, using equation (8). Because $\bar{\rho}$ increases exponentially with z , $\overline{u'w'}$ also increases exponentially with z . Thus, $\overline{u'w'}$ increases by $\sim 10^8$ for GWs propagating from the

troposphere to the lower thermosphere. After a GW reaches z_{diss} , $\overline{u'w'}$ decreases rapidly if λ_z decreases and decreases less rapidly if λ_z continues to increase.

[11] The GWs shown in Figure 3c have $\lambda_H = 400$ km and intrinsic periods of $\tau_{\text{Ir}} = 2\pi/\omega_{\text{Ir}} \sim 35$ min, which are typical of the aurorally generated GWs observed by Bristow et al. [1996]. For $\bar{T} = 1000$ –1500 K, Figure 3c shows that this GW dissipates at $z_{\text{diss}} \simeq 200$ –210 km, with $\lambda_z \simeq 80$ –100 km at z_{diss} . However, this GW is likely to be observed up to $z \sim 250$ km because $\overline{u'w'}$ is still reasonably large there. Bristow et al. [1996] examined this GW using the non-dissipative and dissipative dispersion relations of Hines [1960] and Francis [1973], respectively with $\bar{T} = 1200$. They found that at $z \sim 210$ km, $\lambda_z \simeq 150$ km and 160 km, respectively (see Figures 7 and 8 from Bristow et al. [1996]). In addition, the attenuation distance decreased rapidly only above $z \simeq 230$ km. Thus, Francis' dissipative dispersion relation may result in a larger λ_z and a larger z_{diss} than the dissipative dispersion relation used here.

[12] In deriving this dispersion relation, we made several assumptions. The first is that \bar{T} , the horizontal winds, and ν change “slowly enough” (equation (8) of the work by VF2006). We showed in the work of VF2006 that for most of the GWs originating in the lower atmosphere, the temperature profiles employed here do change slowly enough. We also found that even for very steep wind gradients which do not satisfy the “slowly enough” condition, the ray-trace solutions agree with the exact solutions. Therefore the “slowly enough” criteria may be overly restrictive. The slowly enough condition for ν was estimated to be $\lambda_z \lesssim 2\pi[(d\nu/dz)/\nu]^{-1} \simeq 2\pi(0.71\bar{T}^{-1}d\bar{T}/dz + H^{-1})^{-1}$. However, the ray-trace solutions displayed in Figure 2c in the work of VF2005 showed that this condition is overly restrictive. Therefore the slowly enough condition for ν we adopt here is

$$\lambda_z(z_{\text{diss}}) \lesssim 4\pi [(d\nu/dz)/\nu]^{-1}, \quad (10)$$

although this condition may also be overly restrictive. Here $\lambda_z(z_{\text{diss}})$ is the vertical wavelength of a GW at z_{diss} . For the GWs shown in Figure 3a in temperature profiles II and V, $2\pi[(d\nu/dz)/\nu]^{-1}$ at z_{diss} is ~ 130 and ~ 285 km, respectively, while $\lambda_z(z_{\text{diss}}) \sim 65$ and 100 km, respectively. Therefore ν changes slowly enough for these GWs.

[13] The second assumption we made is that the WKB approximation is satisfied while ray tracing. *Einaudi and Hines* [1970] showed that the WKB approximation is valid as long as the residue is much less than one, where the residue is defined in our notation as

$$R_2 = \frac{1}{2m^3} \frac{d^2m}{dz^2} - \frac{3}{4m^4} \left(\frac{dm}{dz} \right)^2. \quad (11)$$

When $R_2 > 1$, the WKB approximation fails because the solution cannot be written as a single upgoing or downgoing GW. This occurs if dissipation causes an upward propagating GW to partially reflect downward [Midgley and Liemohn, 1966; Yanowitch, 1967; Volland, 1969]. Those portions of the ray solutions where $R_2 \geq 1$ are shown in Figure 3 between the small black circles. For these GWs, the solutions fail well after they dissipate.

3. Properties of Gravity Wave Propagation and Dissipation

[14] In this section, we show many properties of dissipating GWs, such as dissipation altitudes, range of allowed vertical wavelengths, horizontal distances traveled prior to dissipation, and total time taken to travel these distances. These GWs propagate upwards from launch altitudes of $z_i = 0$ (i.e., the lower atmosphere), $z_i = 120$ km (approximate auroral excitation altitude), $z_i = 150$ km, and $z_i = 180$ km (approximate thermospheric body force altitude). The launch altitude $z_i = 180$ km is utilized because it is the approximate altitude where convectively generated GWs dissipate in the thermosphere and create thermospheric body forces (VF2006). These thermospheric body forces likely generate medium and large-scale secondary GWs, and thus may be a new source of MSTIDs and LTIDs which occur during geomagnetically quiet and active conditions.

[15] Because the intrinsic properties of a GW determines its dissipation altitude (VF2005), and because we are only interested in exploring general properties of GW dissipation here, we do not include background winds. However, many of our results are valid when background winds are included, such as the dissipation altitudes and maximum vertical wavelengths achieved prior to dissipation, as long as the intrinsic GW properties at and somewhat below the dissipation altitudes are utilized.

[16] In Figure 4, as functions of the horizontal wavelength $\lambda_H \equiv |2\pi/k_H|$ and the initial vertical wavelength $\lambda_z(z_i)$, we show the dissipation altitudes, z_{diss} , for upward-propagating GWs as pink dash lines, and the maximum GW vertical wavelengths prior to dissipation, $\lambda_z(z_{\text{max}})$, as blue solid lines. Green dot lines show the intrinsic GW periods (at and near the dissipation altitudes), $\tau_{\text{Tr}} = 2\pi/\omega_{\text{Tr}}$. Each GW’s horizontal wavelength is constant with altitude here because we are not allowing for horizontal variations in the background densities, temperature, etc. [Lighthill, 1978]. GWs launched from $z_i = 0$ are shown in the left column, while those GWs launched from $z_i = 120$ km are shown in the right column. The top to bottom rows correspond to temperature profiles II, III, IV, and V, respectively. We also show those GWs which violate equation (9) as dark blue shading, those GWs with $2\pi[(d\nu/dz)/\nu]^{-1} < \lambda_z(z_{\text{diss}}) < 4\pi[(d\nu/dz)/\nu]^{-1}$ with aqua shading, and those GWs with $\lambda_z(z_{\text{diss}}) > 4\pi[(d\nu/dz)/\nu]^{-1}$ as dark green triangular-shaped shading on the left-hand side of each plot. These latter GWs have very large ω_{Tr} , causing them to reflect in the hotter thermosphere; however, they dissipate prior to reflecting, so that $\lambda_z(z_{\text{diss}})$ is very large. We also show those GWs with $R_2 > 1$ after they reach z_{diss} but before their momentum flux amplitudes decrease by a factor of 2 with light pink-grey shading. Because a GW’s momentum flux decreases above z_{diss} , the results in the light pink-grey shaded regions are likely reasonably accurate. However, we discard the results in the dark blue and dark green shaded regions.

[17] General features of Figure 4 include (1) GWs launched from $z_i = 0$ with $\lambda_z(z_i) > 50$ km and $\lambda_H \sim 100$ –400 km dissipate at the highest altitudes, (2) GWs launched from $z_i = 120$ km with $\lambda_z(z_i) > 100$ km and $\lambda_H \sim 150$ –600 km dissipate at the highest altitudes, and (3) GWs penetrate to higher altitudes during active solar conditions than during extreme solar minimum. We show how to utilize the results from Figure 4 by employing an example. Imagine observing an upward-propagating GW at $z \sim 130$ km that has $\lambda_H = 200$ km and an apparent (ground-based) horizontal phase speed of $c_H = 83$ m s⁻¹. Using the relation $c_H = \omega_r/k_H$, where ω_r is the ground-based frequency, the ground-based period $\tau_r = 2\pi/\omega_r$ is calculated to be 40 min. If we neglect background winds, then the intrinsic period is $\tau_{\text{Tr}} = 40$ min. If the thermospheric temperature is 600 K, we use temperature profile II. Assuming that this GW originates in the lower atmosphere, we view Figure 4a. Locating the “ $\lambda_H = 200$ ” tick mark on the x axis and drawing an imaginary vertical line, this line intersects the 40-min intrinsic period green dot line when $\lambda_z(z_i) \simeq 25$ –30 km, the dissipation altitude is $z_{\text{diss}} \sim 150$ km, and the maximum vertical wavelength prior to dissipation, $\lambda_z(z_{\text{max}})$, is $\lambda_z(z_{\text{max}}) \sim 30$ km. A similar result is obtained if this GW was excited at $z_i = 120$ km instead (see Figure 4b), and similar results are obtained if $\bar{T} = 1000, 1500$ or 2000 K (see

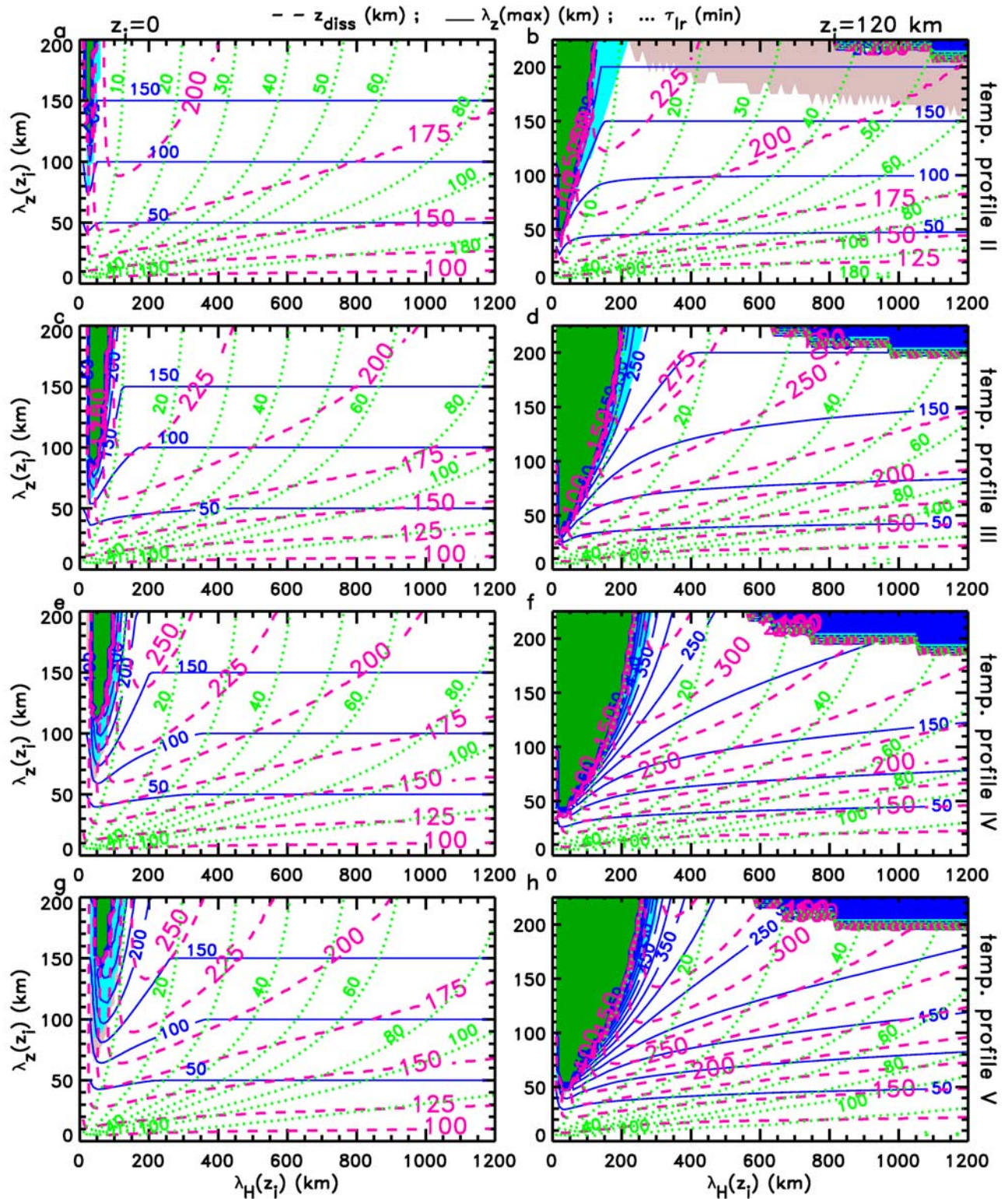


Figure 4. Dissipation properties of GWs when launched from $z_i = 0$ (left column) and $z_i = 120$ km (right column) as functions of λ_H and $\lambda_z(z_i)$. Pink dash lines show GW dissipation altitudes, z_{diss} , in 25-km intervals. Blue solid lines show maximum vertical wavelengths prior to dissipation, $\lambda_z(z_{\max})$, in 50-km intervals. Green dot lines show the GW intrinsic periods, τ_{Ir} , at 10, 20, 30, 40, 50, 60, 80, 100, and 180 min.

Figures 4c–4h). For all temperature profiles, $z_{\text{diss}} \sim 140$ – 150 km and $\lambda_z(z_{\text{max}}) \sim 25$ – 30 km for this GW. Because λ_z is small, z_{diss} does not depend sensitively on the temperature profile because this GW dissipates in the lower thermosphere where the different temperature profiles have similar values. Additionally, $\lambda_z(z_{\text{max}})$ is not very different from $\lambda_z(z_i)$ because $\lambda_z(z_i)$ is relatively small and $\tau_{\text{Ir}} > 15$ – 20 min.

[18] We now show how to utilize the results from Figure 4 if the background winds are known. The intrinsic frequency of a GW is

$$\omega_{\text{Ir}} = \omega_r - kU - lV, \quad (12)$$

where U and V are the background zonal and meridional wind components, respectively, and ω_r is the ground-based GW frequency. If eastward and westward propagating GWs with $\lambda_x = 200$ km and ground-based periods of $\tau_r = 2\pi/\omega_r = 40$ min are observed propagating at $z \sim 100$ km in an eastward zonal wind of $U = 50$ m s $^{-1}$, the eastward propagating GW is Doppler shifted to a smaller intrinsic frequency while the westward propagating GW is Doppler shifted to a larger intrinsic frequency. Using equation (12) and $k = \pm 2\pi/\lambda_x = \pm 3.14 \times 10^{-5}$ m $^{-1}$, the intrinsic frequencies of the eastward and westward propagating GWs are $\omega_{\text{Ir}} = \omega_r - kU = 2\pi/(2400 \text{ s}) \mp 0.0016 \text{ s}^{-1} = 0.001$ and 0.0042 s^{-1} , which implies intrinsic periods of $\tau_{\text{Ir}} = 2\pi/\omega_{\text{Ir}} \simeq 100$ and 25 min, respectively. Assuming a thermospheric temperature of $\bar{T} = 1000$ K and a constant eastward wind of $U = 50$ m s $^{-1}$ above $z \gtrsim 100$ km, we use Figure 4c to estimate the dissipative properties of these GWs. Locating the $\lambda_{\text{H}} = 200$ -km tick mark on the x axis and drawing a vertical line, the intersection of this line with the green dot “100”-min and (interpolated) “25”-min lines yield $z_{\text{diss}} \sim 110$ – 115 km and $\lambda_z(z_{\text{max}}) \sim 10$ – 15 km for the eastward-propagating GWs, and $z_{\text{diss}} \sim 180$ – 190 km and $\lambda_z(z_{\text{max}}) \sim 55$ – 65 km for the westward-propagating GWs, respectively. (Note that when background winds are included, the initial vertical wavelengths on the y axis are not correct and should not be utilized.) Therefore the influence of background winds can be large, allowing much deeper penetration for those GWs moving against the wind with larger intrinsic frequencies (but with $\omega_{\text{Ir}} < N$ to avoid reflection) than those GWs moving into the wind with smaller intrinsic frequencies. In this example, the winds above the observing altitude were assumed constant. If the winds decrease above $z \geq 100$ km however, the intrinsic periods of the westward-propagating GWs will increase, thereby decreasing their dissipation altitude. Therefore, in order to accurately calculate dissipation altitudes using Figure 4, the intrinsic period near or at the dissipation altitude must be known.

[19] In addition to displaying z_{diss} and $\lambda_z(z_{\text{max}})$, Figure 4 displays the range of vertical wavelengths each GW has for $z \leq z_{\text{diss}}$ (excepting the decrease of λ_z in the mesosphere and lower thermosphere). For example, an upward-propagating GW excited by auroral heating at $z_i = 120$ km in temperature profile V with $\lambda_{\text{H}} = 600$ km, $\lambda_z(z_i) = 80$ km, and $\tau_{\text{Ir}} \sim 40$ min has a range of vertical wavelengths of $\lambda_z(z) \simeq 80$ – 125 km along its raypath up to $z = z_{\text{diss}}$, using Figure 4h.

[20] In addition to vertical aspects of GW dissipation in the thermosphere, there are horizontal aspects as well because these GWs travel horizontally and vertically simul-

aneously. In Figure 5, we show the horizontal distances traveled from the launch location until the GWs dissipate, X_{diss} , as reddish-brown dash lines, the intrinsic horizontal phase speeds, $c_{\text{IH}} \equiv \omega_{\text{Ir}}/k_{\text{H}}$, as yellow solid lines, and the total times taken to reach z_{diss} from the launch location, t_{diss} , as blue dot lines for the same internal, upward-propagating GWs shown in Figure 4. The columns, rows, and shading are the same as in Figure 4. The launch altitude $z_i = 120$ km can either be utilized as the altitude where the GWs are created or as the altitude where the GWs (or TIDs) are observed propagating within the thermosphere. As an example of the latter usage, if an upward propagating GW (excited at any altitude below 120 km) is observed at $z \sim 120$ km with $\lambda_{\text{H}} = 400$ km and $c_{\text{IH}} \simeq 200$ m s $^{-1}$ in a thermosphere with $\bar{T} = 1000$ K, then from Figure 5d, the time taken to dissipate from that altitude is $t_{\text{diss}} \sim 1$ hour, and the horizontal distance traveled during that time is $X_{\text{diss}} \sim 500$ km. We can determine the dissipation altitude as well by locating the corresponding value of $\lambda_z(z_i)$ on the y axis in Figure 5d, locating this same value in Figure 4d, then finding where it intersects the $\lambda_{\text{H}} = 400$ km vertical line in Figure 4d. In this case, $\lambda_z(z_i) \simeq 60$ km, so this GW dissipates at $z_{\text{diss}} \simeq 200$ km.

[21] What limits a GW’s ability to propagate large distances horizontally is the duration of time it propagates vertically before dissipating, which is partially determined by its vertical group velocity $c_{\text{g},z} = \partial\omega_{\text{Ir}}/\partial m$. If the same GW in the previous example has twice the horizontal wavelength instead (i.e., $\lambda_{\text{H}} = 800$ km), then the time taken to dissipate from $z_i = 120$ km is longer, $t_{\text{diss}} \sim 100$ min, and the horizontal distance traveled during that time is also longer, $X_{\text{diss}} \sim 850$ km, even though the dissipation altitude is lower, $z_{\text{diss}} \simeq 180$ km. This occurs because the former GW has a larger ω_{Ir} than that of the latter GW and therefore propagates upwards more quickly because of its faster vertical group velocity $c_{\text{g},z} \sim \lambda_z\omega_{\text{Ir}}/2\pi$. Here $\lambda_z(z_i)$ is approximately the same for both GWs. The larger $c_{\text{g},z}$ for the former GW shortens t_{diss} and therefore shortens X_{diss} , since the horizontal group velocity, $c_{\text{g},\text{H}} = \partial\omega_{\text{Ir}}/\partial k_{\text{H}} \sim \lambda_z N/2\pi$, is nearly the same for both GWs.

[22] Therefore upward-propagating, aurorally generated GWs which travel large horizontal distances prior to dissipating have small $c_{\text{g},z}$, large λ_{H} , and sufficiently large λ_z (in order that they penetrate into the lower thermosphere before dissipating). This effect is observed in the right-hand column of Figure 5; for $\lambda_z(z_i) > 40$ km, $c_{\text{IH}} \geq 150$ m s $^{-1}$, and $\lambda_{\text{H}} \geq 100$ km, X_{diss} is approximately proportional to λ_{H} (that is, if λ_{H} is larger, then X_{diss} is larger). Additionally, for those GWs with large λ_{H} , those with the largest values of $\lambda_z(z_i)$ travel the largest horizontal distances. Comparing Figures 5 and 4, large λ_{H} generally corresponds to large τ_{Ir} . Thus, GWs with large λ_{H} and τ_{Ir} tend to travel large horizontal distances prior to dissipating. The result that long period, high phase speed GWs travel large horizontal distances before dissipating was shown previously [Richmond, 1978; Walker et al., 1988; Hocke and Schlegel, 1996]. For $\lambda_{\text{H}} \simeq 1200$ km, the largest horizontal distance traveled is $X_{\text{diss}} \simeq 1250$ km for GWs launched from $z_i \simeq 120$ km, using Figure 5. Extending these results out to $\lambda_{\text{H}} \simeq 3000$ km, the largest horizontal distances traveled are instead double, $X_{\text{diss}} \simeq 2500$ km (not shown). These results are consistent with the observational result that TIDs tend to propagate less than a

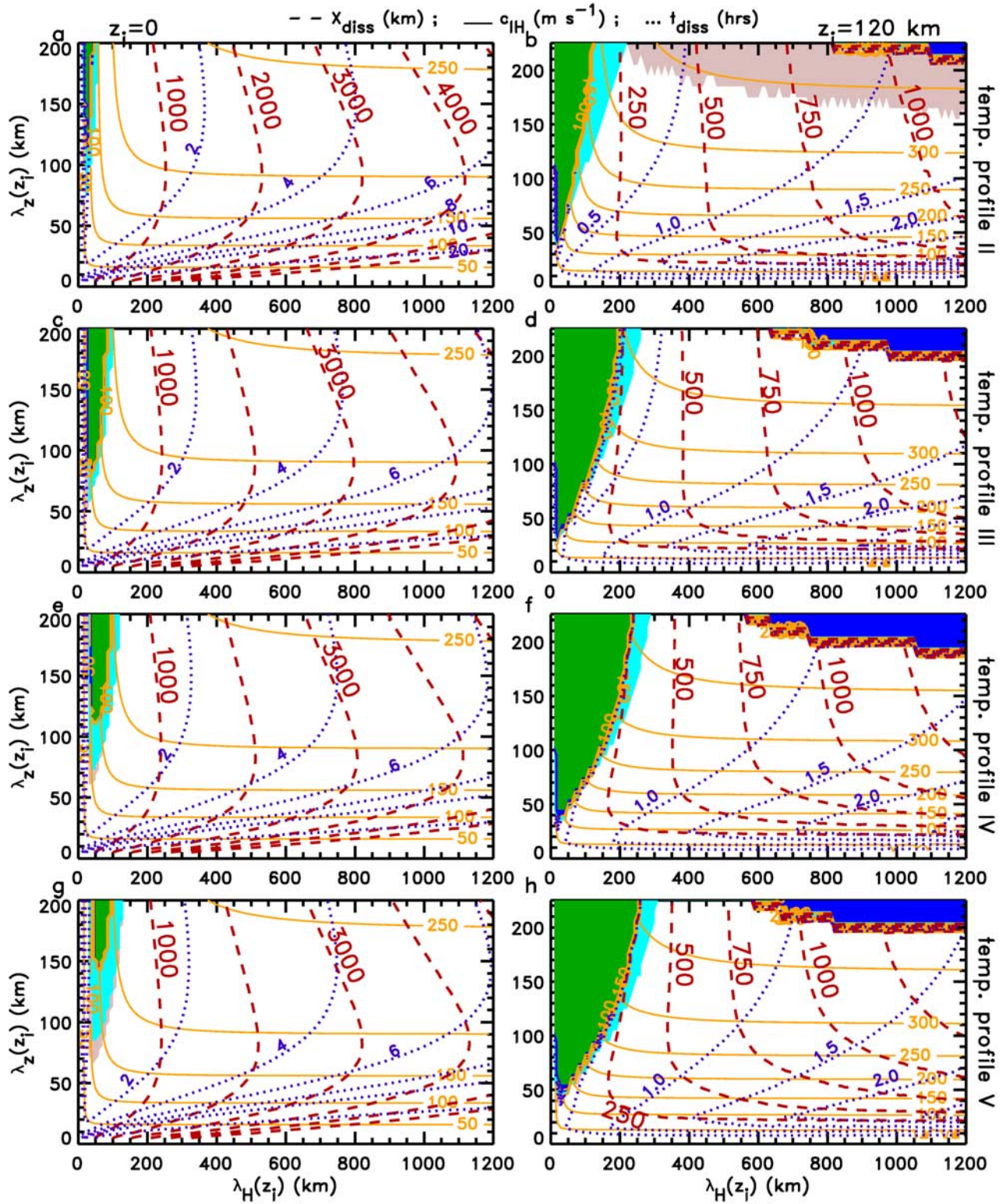


Figure 5. Dissipation properties for the same GWs shown in Figure 4. Reddish-brown dash lines show the horizontal distances traveled while these GWs propagated from $z = z_i$ to $z = z_{\text{diss}}$, X_{diss} , in 1000-km intervals up to 6000 km (left column) and 250-km intervals (right column), as labeled. Blue dot lines show the times taken to dissipate, t_{diss} , at 2, 4, 6, 8, 10, and 20 hours (left column) and in 0.5 hour intervals (right column). Yellow solid lines show the intrinsic horizontal phase speeds, c_{IH} , in 50 m s^{-1} intervals.

quarter of the way around the Earth (which is about 10,000 km). However, downward-propagating GWs excited in the thermosphere may reflect from the Earth and propagate upwards into the thermosphere prior to dissipating, therefore traveling much longer horizontal distances than those shown here. Although we are not considering Earth-reflected GWs here, they can be important (see below).

[23] The left columns of Figures 4 and 5 show that small- and medium-scale GWs with $\lambda_H < 500$ km, $c_{IH} \geq 100$ m s⁻¹, and $\tau_{Ir} < 60$ min propagate less than ~ 2000 km horizontally from the ground prior to dissipating at $z_{diss} \sim 150$ –250 km. This suggests that if GWs from a tropospheric source propagate into the thermosphere, the corresponding MSTIDs will not be observed more than ~ 2000 km from this source. This result is consistent with those of *Waldock and Jones* [1987], who showed that most MSTIDs could be reverse ray-traced back to tropospheric altitudes within 250–1500 km horizontally of the observation location. Our result for z_{diss} is also consistent with the mostly daytime observations of *Waldock and Jones* [1986], who observed medium-scale GWs in the F region with horizontal phase speeds of 100–200 m s⁻¹ and periods of 10–30 min.

[24] GWs excited from the aurora and observed by oblique HF radar have ground-based periods of $\tau_r \simeq 20$ –50 min, $\lambda_H \simeq 200$ –450 km, and $c_H = 100$ –200 m s⁻¹ and are often observed propagating more than 1000 km from their source region 2000 km away [*Bristow et al.*, 1996]. Many of these GWs are believed to be Earth-reflected [*Samson et al.*, 1989, 1990; *Bristow et al.*, 1994]. The right columns of Figures 4 and 5 show that if these medium-scale GWs are upward-propagating, they would not propagate more than 600 km from the source at $z_i = 120$ km. However, if these GWs instead propagated downward, reflected at the Earth's surface, then propagated upwards, they would travel horizontally $\sim 2 \times (1000$ –2000) km ~ 2000 –4000 km prior to dissipating in the thermosphere (see the left column of Figure 5). Therefore our estimate based on this new dispersion relation is consistent with these observational results.

[25] As discussed previously, we also consider the propagative and dissipative properties of upward-propagating GWs launched from higher altitudes within the thermosphere. For upward-propagating GWs that are launched from $z_i = 150$ km (left column) and $z_i = 180$ km (right column), Figure 6 shows the dissipation altitudes and maximum vertical wavelengths, while Figure 7 shows the horizontal distances traveled and the total time taken to reach z_{diss} from z_i . We use the same linetypes, colors, and shading as in Figures 4 and 5. As before, the top to bottom rows correspond to temperature profiles II, III, IV, and V, respectively. Note that *Volland* [1969] showed that reflection is negligible for a GW with $\lambda_x \simeq 300$ km and wave period of 21 min. This agrees with our results, as this GW is outside the light pink-grey shaded regions in Figure 6.

[26] Figures 6 and 7 are utilized the same way as Figures 4 and 5 to obtain z_{diss} , $\lambda_z(z_{max})$, X_{diss} , and t_{diss} . As before, the launch altitudes z_i can either be utilized as the altitudes where the GWs are created or as the altitudes where upward-propagating GWs are observed. As an example, consider an upward-propagating GW with $\lambda_H = 1000$ km and $\tau_{Ir} = 60$ min, which is observed at $z = 150$ km in a thermosphere with $\bar{T} = 1000$ K. Using Figures 6c and 7c,

this GW dissipates at $z_{diss} \sim 210$ km, has a range of vertical wavelengths $\lambda_z = 100$ –120 km for 150 km $\leq z \leq 210$ km, has an intrinsic horizontal phase speed $c_{IH} \sim 275$ m s⁻¹, travels horizontally $X_{diss} \sim 600$ –650 km before dissipating, and takes $t_{diss} \sim 1$ hour to dissipate from $z_i = 150$ km.

[27] Figure 6b shows that many GWs launched from $z_i = 180$ km dissipate within a scale height during extreme solar minimum, with $z_{diss} \simeq 250$ km being the maximum attainable altitude. During very active solar conditions, however, the maximum attainable altitude from the same launch altitude is much higher, up to $z_{diss} \sim 450$ km (see Figure 6h). However, even during very active solar conditions, those GWs with $\lambda_z(z_i) \lesssim 100$ km dissipate just above $z_i = 180$ km. For example, a GW with $\lambda_H \sim 900$ km and $\tau_{Ir} \simeq 60$ min dissipates at $z_{diss} \sim 200$ km regardless of its launch altitude (see Figures 4h, 6g, and 6h).

[28] For GWs launched from the thermosphere, those with large λ_H and $\lambda(z_i)$ travel the largest horizontal distances. As before, GWs with larger τ_{Ir} tend to propagate larger horizontal distances X_{diss} than GWs with smaller τ_{Ir} . Therefore, because of wave dissipation in the vertical direction, as a GW packet propagates away from an auroral source, GWs with smaller τ_{Ir} tend to be spectrally filtered out, causing the dominant wave period of the wave packet to increase with time and distance away from the source. This result is consistent with observational and theoretical results of Earth-reflected GWs [*Bristow and Greenwald*, 1996].

[29] One of the striking features of Figures 4, 5, 6, and 7 is that lines of constant τ_{Ir} are oriented in a similar manner to lines of constant t_{diss} for GWs with large enough c_{IH} . For GWs launched from $z_i = 120$ km with $\tau_{Ir} \sim 20$ –100 min and $c_{IH} > 100$ m s⁻¹, $t_{diss}/\tau_{Ir} \sim 1$ –2. For GWs launched from $z_i = 180$ km with $\tau_{Ir} \sim 20$ –60 min and $c_{IH} > 300$ m s⁻¹, $t_{diss}/\tau_{Ir} \sim 0.5$ –1.5. This implies that upward-propagating GWs generated in the thermosphere will typically only cycle through one half to two wave cycles prior to dissipating. Thus, upward-propagating GWs generated in the thermosphere may appear quasiperiodic, with significantly decreasing amplitudes over a wave cycle or two.

[30] *Shiokawa et al.* [2006] observed quasiperiodic southward-moving waves in their OI 630-nm airglow images at Kototabang, Indonesia (altitude range 200–300 km), which they argued may have been GWs. Typical waves had $\tau_r \simeq 40$ min and $c_H \simeq 310$ m s⁻¹. From Figures 4 and 5, a GW with $c_H \simeq 310$ m s⁻¹ and $\tau_{Ir} \sim 40$ –50 min cannot originate in the lower atmosphere unless the horizontal winds are > 60 m s⁻¹, since $c_{IH} = c_H - U_H$ from equation (12). Here U_H is the component of the horizontal background wind along the propagation direction of the GW. Alternatively, GWs with $\tau_{Ir} \simeq 40$ min and $c_{IH} \simeq 310$ m s⁻¹ can be excited in the thermosphere. Since the observed GWs do not correlate with the Kp index, it is unlikely that these waves were excited by geomagnetic processes. Because the waves observed in this study were most frequently observed in May to July, which is the Asian monsoon season, and because the waves are medium to large scale, it is possible that during this time, small-scale GWs excited from the monsoon dissipated in the thermosphere, creating thermospheric body forces at $z \sim 150$ –250 km in a manner similar to that discussed in the work of VF2006. These body forces then would have excited medium and large-scale secondary

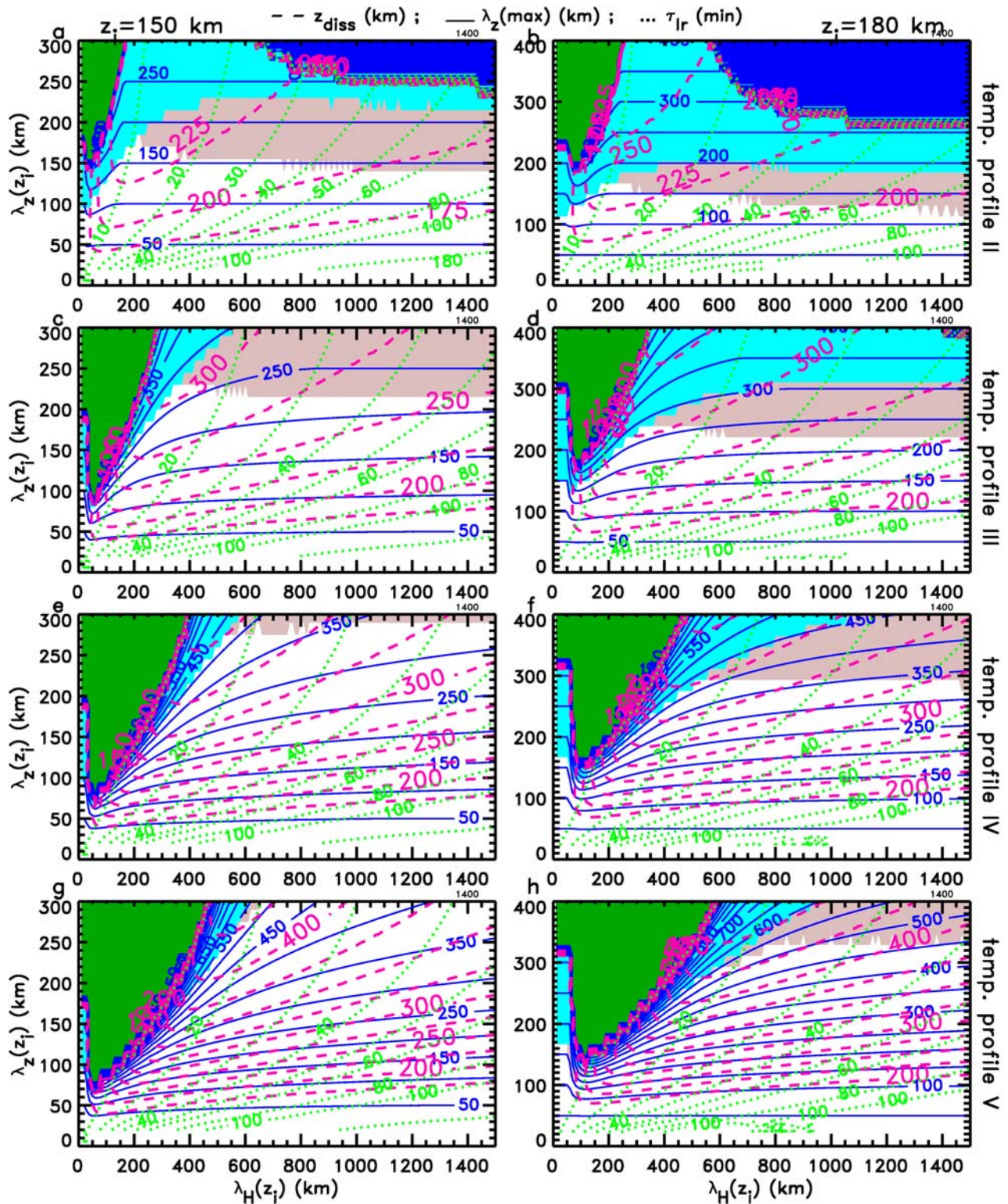


Figure 6. Same as in Figure 4 but for GWs launched from $z_i = 150$ km (left column) and $z_i = 180$ km (right column). Pink dash lines show z_{diss} in 25-km intervals, blue solid lines show $\lambda_z(z_{max})$ in 50-km intervals, and green dot lines show τ_{ir} in minutes with the same values as in Figure 4.

GWs with periods and wavelengths similar to those observed here. Regardless of the source, if this GW was excited at $z_i = 150$ – 180 km, and if we assume that the background winds were small, then $\tau_{ir} \simeq 40$ min and $c_{IH} \sim 310$ m s⁻¹.

Then using Figures 6 and 7, $\lambda_H \sim 700$ km, $\lambda_z(z_i) \sim 100$ – 120 km, $\lambda_z(z_{max}) \simeq 110$ – 160 km, and $z_{diss} \sim 200$ – 250 km. A larger (smaller) intrinsic frequency (because of background winds) results in higher (lower) dissipation altitudes.

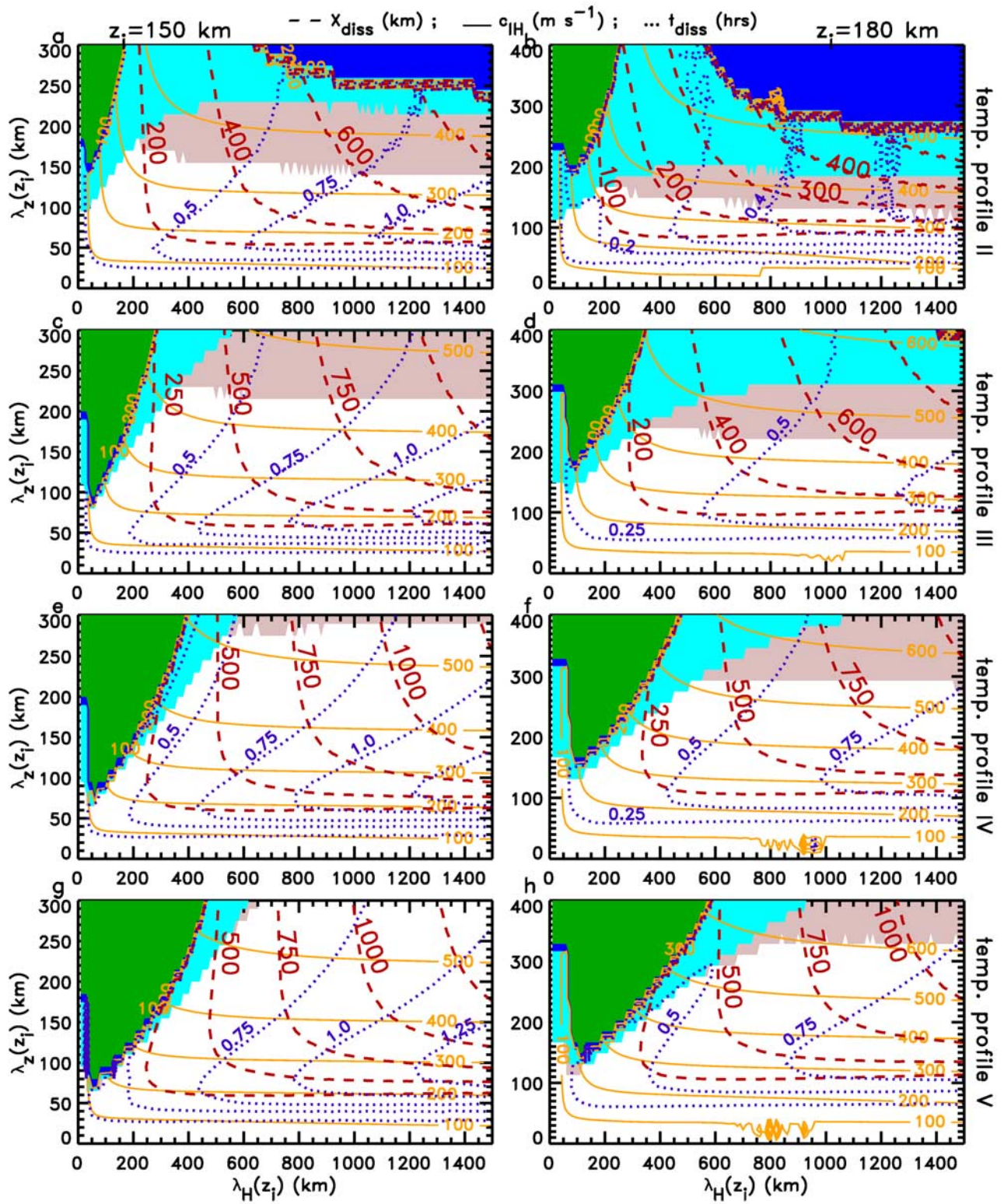


Figure 7. Same as in Figure 5 but for GWs launched from $z_i = 150$ km (left column) and $z_i = 180$ km (right column). (a, d) Reddish-brown dash lines show X_{diss} in 200-km intervals, (b) 100-km intervals, (c, e–h) and 250-km intervals, as labeled. Blue dot lines show t_{diss} in (a, c–h) 0.25-hour intervals and (b) 0.1-hour intervals, as labeled. Yellow solid lines show c_{gH} in 100 m s^{-1} intervals.

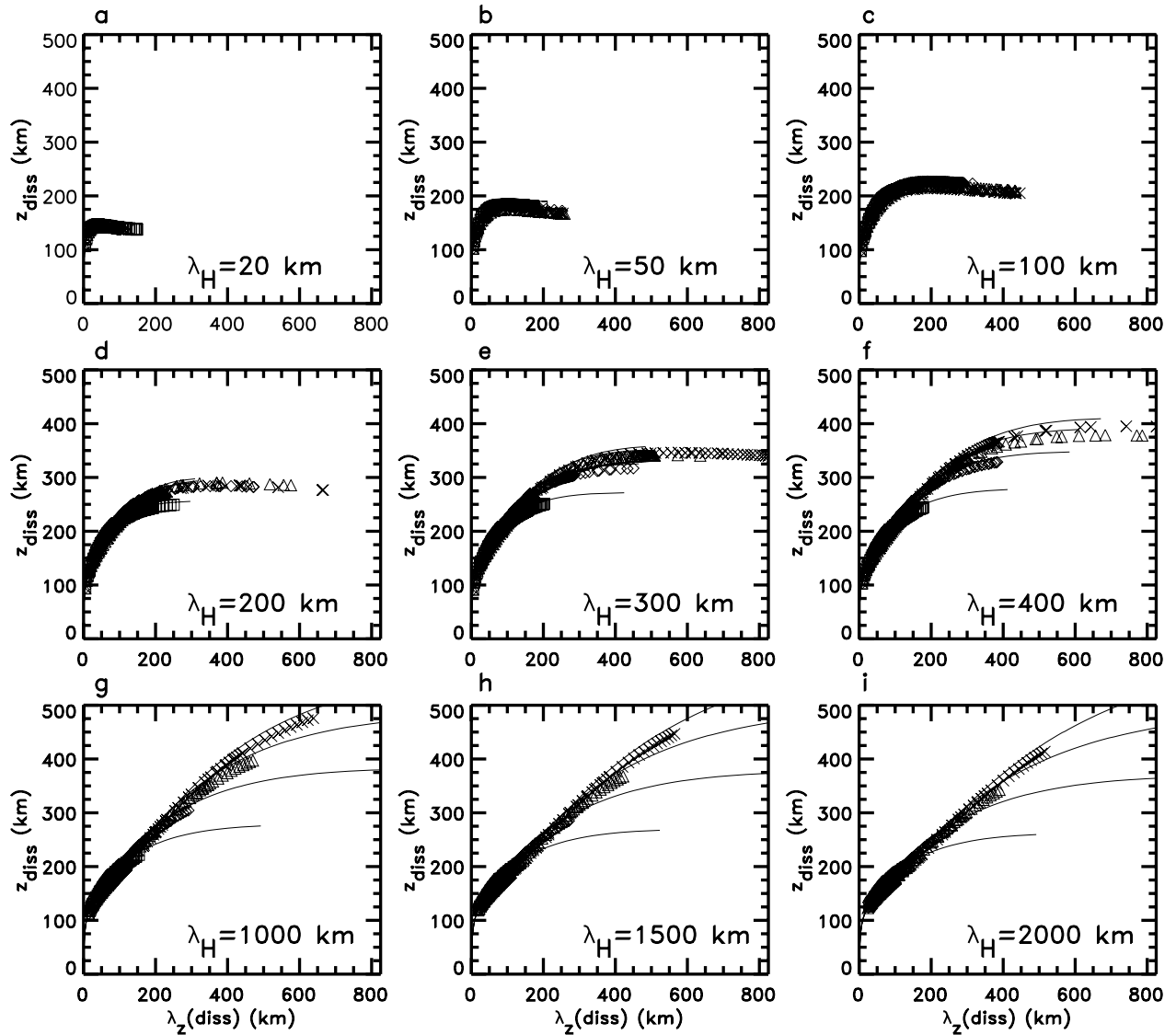


Figure 8. GW vertical wavelengths at the dissipation altitudes, $\lambda_z(z_{\text{diss}})$, as a function of the GW dissipation altitudes, z_{diss} , for GWs with $\lambda_H =$ (a) 20, (b) 50, (c) 100, (d) 200, (e) 300, (f) 400, (g) 1000, (h) 1500, and (i) 2000 km. Each plot includes all of the launch altitudes $z_i = 0, 120, 150,$ and 180 km. Results for temperature profiles II, III, IV, and V are shown as squares, diamonds, triangles, and Xs, respectively. The solid lines show the solutions of the dissipation condition, equation (13). These lines are not visible in Figures 8a–8c because they overlap with the symbols.

Because this GW's c_{IH} is large, only background winds $\geq 50 \text{ m s}^{-1}$ can appreciably change z_{diss} . This is possible, however, because horizontal thermospheric winds up to $100\text{--}200 \text{ m s}^{-1}$ can occur daily. Note that these dissipation altitudes are consistent with the observation that these GWs were not observed equatorward of the anomaly (i.e., at higher altitudes) [Shiokawa *et al.*, 2006].

4. Spectra of Dissipating Gravity Waves With Altitude

[31] In the last section, we presented key dissipation parameters for a wide variety of individual, upward-propagating GWs in the thermosphere. Because GWs dissipate at differing altitudes in the thermosphere, with GWs having smaller (larger) λ_z dissipating at lower (higher)

altitudes, a GW packet will be dissipatively filtered as it travels upwards in the thermosphere, shifting to larger λ_z as it propagates. We combine the results of individual GWs in this section, in order to determine if there are general trends for λ_z , λ_H , and τ_{Ir} with altitude for the dissipating GWs. This also allows for comparison with observations.

[32] Figure 8 shows $\lambda_z(z_{\text{diss}})$ as a function of the dissipation altitudes, z_{diss} , using the results for all of the launch altitudes from Figures 4 and 6 for GWs with $\lambda_H = 20, 50, 100, 200, 300, 400, 1000, 1500,$ and 2000 km. The squares, diamonds, triangles, and Xs denote GWs which propagate within temperature profiles II, III, IV, and V, respectively. We do not include those GWs which violate equations (9) and (10), dissipate within $H/2$ of the launch altitude or have intrinsic periods $\tau_{\text{Ir}} > 6$ hours. This last condition eliminates large-scale, shallow GWs which dissipate near

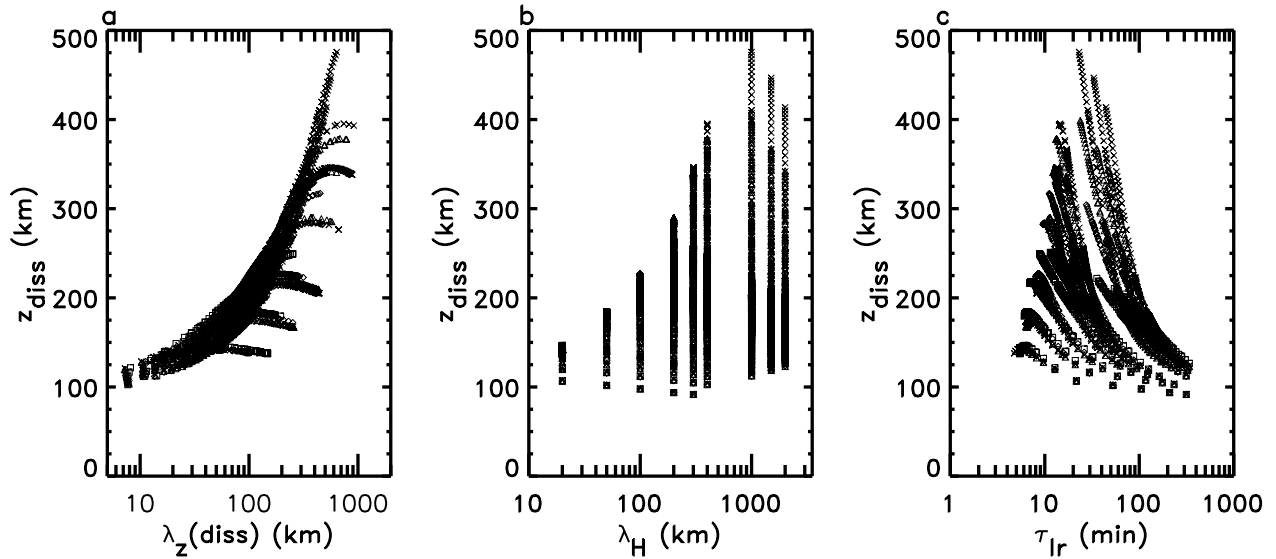


Figure 9. (a) Vertical wavelengths $\lambda_z(z_{\text{diss}})$ as a function of z_{diss} for all of the dissipating GWs shown in Figure 8 at all launch altitudes. (b) Horizontal wavelengths λ_H as a function of z_{diss} for the dissipating GWs in Figure 9a. (c) Intrinsic periods as a function of z_{diss} for the dissipating GWs in Figure 9a. The symbols are the same as in Figure 8.

the turbopause (for example, dissipation altitudes less than $z < 115$ km when $\lambda_H = 2000$ km in Figure 8i). We see that $\lambda_z(z_{\text{diss}})$ increases linearly with z_{diss} for a fixed value of λ_H . This increase occurs as ω_{Ir} and $\lambda_z(z_i)$ increase for differing GWs in the spectrum. If ω_{Ir} is near N (as occurs for some GWs with $\lambda_H \leq 400$ km and large z_{diss}), then $\lambda_z(z_{\text{diss}})$ increases rapidly with z_{diss} and appears to reach “altitudinal ceilings” that are different for each value of λ_H . This latter behavior does not occur for GWs with $\lambda_H \geq 1000$ km because $\omega_{\text{Ir}} \ll N$ (see Figures 4 and 6). Note that this rapid increase of λ_z with z occurs mainly within the aqua regions in Figures 4 and 6.

[33] Although the curves for differing thermospheric temperatures are similar for fixed λ_H , they are not identical; when the thermosphere is hotter, GWs with the same values of λ_H and $\lambda_z(z_{\text{diss}})$ typically dissipate at somewhat higher altitudes than when the thermosphere is cooler, especially when ω_{Ir} nears N . For example, GWs with $\lambda_H = 300$ km and $\lambda_z(z_{\text{diss}}) \simeq 200$ km dissipate at $z \sim 250$ km during extreme solar minimum and at $z \sim 300$ km during active solar conditions (see Figure 8e). This behavior can be explained theoretically. In the work of VF2006, we derived an approximate expression for GWs which dissipate from kinematic viscosity and thermal conductivity. This dissipation condition is

$$\nu(z_{\text{diss}}) \simeq \frac{|k_H m| N}{2H (\mathbf{k}^2 + 1/4H^2)^{5/2}}, \quad (13)$$

which is solved iteratively for the absolute value of the vertical wave number $m_a = 2\pi/\lambda_z$:

$$m_a = \sqrt{\left(\frac{k_H N}{2H\nu}\right)^{2/5} m_a^{2/5} - k_H^2 - \frac{1}{4H^2}}, \quad (14)$$

where the first guess for m_a on the right-hand side of equation (14) is

$$m_a = \sqrt{\sqrt{\frac{k_H N}{2H\nu} - k_H^2} - \frac{1}{4H^2}}, \quad (15)$$

and succeeding results are substituted in as guesses until convergence in m_a is obtained (equations (23), (24), and (25) from the work of VF2006). These results are shown in Figure 8 as solid lines. The dissipation condition is seen to agree with the ray-trace results very well; the increase of λ_z with z in the linear and rapidly increasing regimes are reproduced, as well as the increase of z_{diss} for increasing \bar{T} when λ_H and $\lambda_z(z_{\text{diss}})$ are fixed. From equation (13), the dissipation condition implies that $\nu H/N$ is approximately constant for GWs with the same m and k_H and which satisfy $m^2 \gg k^2 + 1/4H^2$. Because of the exponential dependence of ν on z/H , the variation of ν is more important than the variations of H or N . Since ν is much smaller in a hot than in a cool thermosphere at the same altitude, we estimate that GWs with the same k_H and $\lambda_z(z_{\text{diss}})$ dissipate at somewhat higher altitudes in hot than in cool thermospheres. This is the observed behavior in Figure 8.

[34] For all of the small, medium, and large-scale GWs displayed in Figure 8, we show $\lambda_z(z_{\text{diss}})$, λ_H , and τ_{Ir} for these dissipating GWs as functions of z_{diss} in Figure 9. Figure 9a shows that the $\lambda_z(z_{\text{diss}})$ versus z_{diss} curves are quite similar for GWs with differing values of λ_H and $\omega_{\text{Ir}} \ll N$. This implies a general relationship between $\lambda_z(z_{\text{diss}})$ and z_{diss} for GWs with $\omega_{\text{Ir}} \ll N$, regardless of λ_H (note that GWs with $\omega_{\text{Ir}} \simeq N$ have much larger $\lambda_z(z_{\text{diss}})$ at any given altitude). We also see that overall, $\lambda_z(z_{\text{diss}})$ increases exponentially with altitude, although with a smaller slope for $z > 200$ km. Figure 9b–9c shows that the highest dissipation altitudes of $z \sim 400$ – 500 km are achieved only for GWs with horizontal wavelengths of $\lambda_H \sim 400$ – 2000 km and

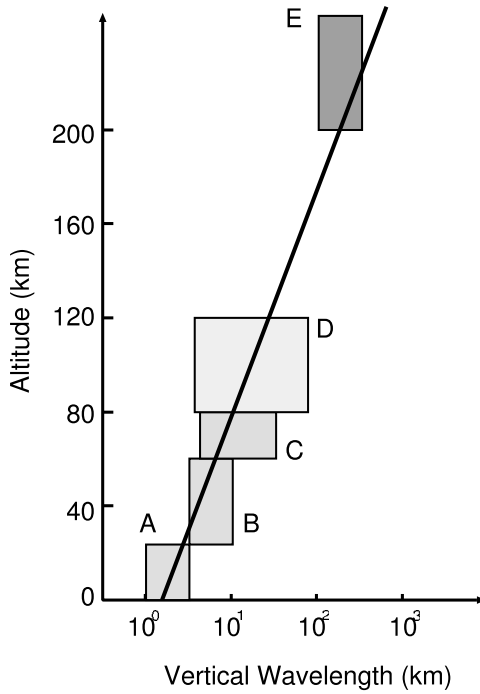


Figure 10. Figure 10 from the work of *Oliver et al.* [1997] showing the observed GW vertical wavelengths as a function of altitude for the MU radar in Japan. Reproduced by permission of the American Geophysical Union.

intrinsic periods of $\tau_{\text{Ir}} \sim 10\text{--}50$ min. Additionally, GWs with small horizontal wavelengths of $\lambda_{\text{H}} \lesssim 20$ km do not dissipate above $z \simeq 150$ km. Finally, there is a clear filtering with respect to intrinsic wave period with altitude; GWs with intrinsic periods of $\tau_{\text{Ir}} \leq 7$ min and $\tau_{\text{Ir}} \geq 300$ min do not dissipate above $z \simeq 150$ km because of reflection and dissipative filtering, respectively.

[35] The exponential increase of λ_z as a function of altitude seen in Figure 9a has been noted up to altitudes of 240 km [*Oliver et al.*, 1997]. In Figure 10, we reprint Figure 10 from the work of *Oliver et al.* [1997], which shows observed daytime GW vertical wavelengths as a function of altitude measured by the MU radar system in Japan. Note the logarithmic x axis and linear y axis (as in our Figure 9a).

[36] In Figure 11, we show the GW dissipation altitudes, z_{diss} , binned as a function of the vertical wavelengths, $\lambda_z(z_{\text{diss}})$, for the same GWs shown in Figure 8. Here we show the results for all four temperature profiles separately, with each plot including all four launch altitudes. As discussed previously, higher penetration altitudes are achievable for GWs propagating in hotter thermospheres. For temperature profiles II, III, IV, and V, the highest dissipation altitudes are 275, 350, 400, and 500 km, respectively. These highest altitudes are only obtained for GWs launched from $z_i = 180$ km rather than from $z_i = 0$ (see Figures 4 and 6). We also show the binned and averaged values of $(z_{u'w'/2} - z_{\text{diss}})/H$ in Figure 11 with grey-scale shading, where white (dark grey) bins denote values of zero (one). Here $z_{u'w'/2}$ is the altitude above z_{diss} where $u'w'$ decreases by a factor of two from its maximum at z_{diss} . Because most of the bins show values of $(z_{u'w'/2} - z_{\text{diss}})/H \simeq$

0.5–1, most GWs reach $z_{u'w'/2}$ approximately $\frac{1}{2} - 1$ scale heights above z_{diss} . Therefore we expect most GWs to be observable up to $\sim 1\text{--}2$ scale heights above z_{diss} , i.e., to altitudes of $z \sim z_{\text{diss}} + (1\text{--}2)H$. For example, an aurorally generated GW with $\lambda_{\text{H}} = 400$ km and $\tau_{\text{Ir}} = 35$ min in temperature profile III has a maximum momentum flux (i.e., dissipates) at $z_{\text{diss}} = 200$ km (see Figure 3c). Because $H \simeq 30$ km at that altitude (see Figure 2c), this GW is expected to be observable up to altitudes of $z \sim 240\text{--}280$ km. This is verified for this GW in Figure 3f.

[37] We overlay in Figure 11 the observational results of *Oliver et al.* [1997] for $z \geq 80$ km, boxes D and E from Figure 10, as dash boxes. We also overlay the observational results of *Djuth et al.* [1997, 2004], who observed GWs with $\lambda_z \simeq 4\text{--}50$ km for $z = 115\text{--}160$ km and $\lambda_z \sim 100\text{--}300$ km for $z = 170\text{--}500$ km at Arecibo Observatory. We plot these results as dash-dot boxes. The observational results agree with the theoretical results fairly well for thermospheric temperatures of $\bar{T} \simeq 600\text{--}1000$ K. Finally, we overlay the solid line in Figure 10 (the “fit” line from the work of *Oliver et al.* [1997]) as long dash lines in Figure 11. Although this line matches the slope well for GWs with $\lambda_z \leq 100$ km and $z_{\text{diss}} < 200$ km, it does not match the slope well for GWs with larger vertical wavelengths when $z > 200$ km, because the growth of λ_z with z when $z > 200$ km is slower than this line implies. Indeed, the slower increase of λ_z with z can even be seen in Figure 10 because this line cuts through only the lower right-hand portion of box E.

[38] In Figure 12, we show $\lambda_z(z_{\text{diss}})$ as a function of z_{diss} binned into shaded boxes for the GWs from Figure 11b. The grey-scale shading shows the average horizontal phase speed for the GWs in each bin. We also overlay the observational results of *Oliver et al.* [1997] and *Djuth et al.* [1997, 2004] as dash and dash-dot boxes, respectively.

[39] Figure 12a shows the results for GWs with all values of λ_{H} and for all four launch altitudes. The agreement between observation and theory is generally very good, as mentioned previously. At $z \sim 80\text{--}120$ km, the agreement is very good except for those GWs with $\lambda_z \sim 20\text{--}80$ km, which were observed but which do not appear in the theoretical boxes. This deficit occurs for several reasons. The first is that we limited our results to those GWs with intrinsic periods smaller than 6 hours; however, large-scale GWs with $\lambda_{\text{H}} \sim 1000$ km, $\tau_{\text{Ir}} > 6$ hours, and $\lambda_z \lesssim 50$ km, for example, likely dissipate at $z \sim 90\text{--}110$ km (see Figure 8g). The second reason is that the theoretical boxes in Figure 12 only display GWs which are dissipating. GWs with vertical wavelengths larger than 20 km (but that dissipate at higher altitudes) can be observed at $z \sim 100\text{--}120$ km if their amplitudes are large enough. Using a GW spectrum from a convective plume model, we show in the next section that GWs up to $\lambda_z \sim 70$ km can be observed at $z \sim 80\text{--}100$ km.

[40] For $z = 115\text{--}160$ km, the theoretical and observational results also agree very well in Figure 12a. For $z = 170\text{--}200$ km, the agreement between theory and both sets of observations is good for most GWs. However, the observations do not include GWs with $\lambda_z = 30\text{--}100$ km for $z = 170\text{--}200$ km that are predicted to be dissipating at these altitudes. This likely occurs because of spectral Doppler-shifting because of the presence of large thermospheric winds, as we show in the next section. Finally, for

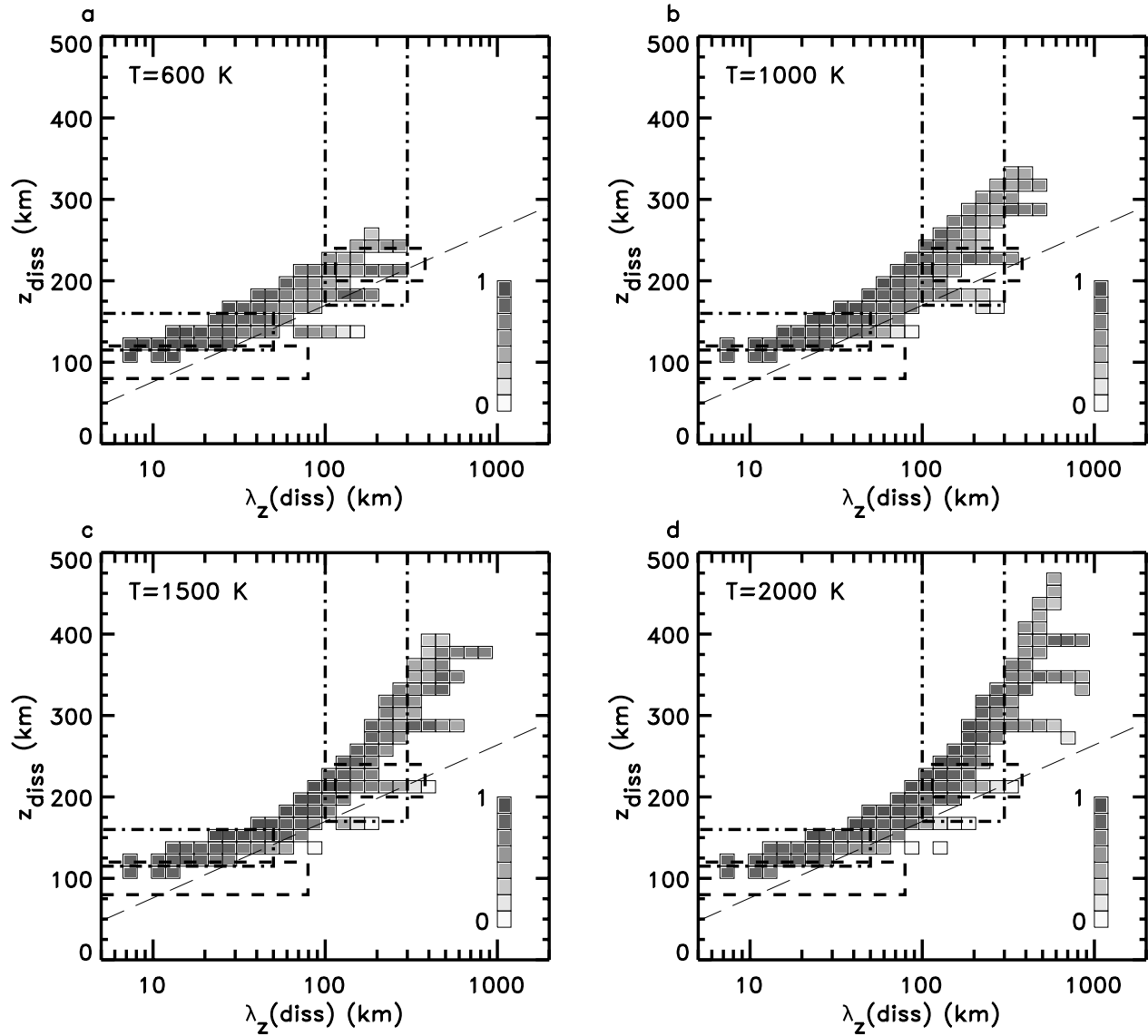


Figure 11. GW dissipation altitudes, z_{diss} , binned as a function of the vertical wavelengths, $\lambda_z(z_{\text{diss}})$, for the GWs shown in Figure 8. GWs in temperature profiles (a) II, (b) III, (c) IV, and (d) V. The grey-scale shading indicates the average value of the quantity, $(z_{\text{diss}} - z_{\text{diss}}^{\text{theoretical}})/H$, binned in intervals of 0.125 from 0 to 1.0, as indicated by the color bar in the lower right hand corner of each plot.

the $z = 200\text{--}325$ km altitude range, theory and observation agree quite well. Note that the GWs with the largest horizontal phase speeds of $c_H \simeq 300\text{--}600$ m s $^{-1}$ dissipate at the highest altitudes of $z \geq 200$ km. Additionally, those GWs with the smallest horizontal phase speeds of $c_H < 50$ m s $^{-1}$ dissipate at $z < 160$ km with small vertical wavelengths of $\lambda_z(z_{\text{diss}}) < 10$ m s $^{-1}$.

[41] Figure 12b shows the theoretical results for GWs with $\lambda_H = 20\text{--}400$ km launched from the lower atmosphere (note that this plot looks the same if all GWs with $\lambda_H = 20\text{--}2000$ km are included instead (not shown)). These small- and medium-scale GWs overlap reasonably well with observations at $z \simeq 80\text{--}160$. However, many of these GWs dissipate at $z \sim 170\text{--}200$ km with $\lambda_z = 30\text{--}100$ km, seemingly inconsistent with observations. However, the background winds were assumed zero here. In a zero-wind environment, the vertical wavelengths of most GWs

launched from the lower atmosphere do not become very large in the thermosphere because the increase of λ_z in the lower thermosphere mostly offsets the decrease of λ_z near the mesopause (however, λ_z for GWs with $\omega_{\text{tr}} \sim N$ increases significantly just prior to dissipation and reflection). Horizontal winds, however, can substantially alter λ_z . For GWs with $m^2 > k_H^2 + 1/4H^2$ and where dissipation is unimportant, the GW dispersion relation becomes

$$\lambda_z \simeq \lambda_H \omega_{\text{tr}} / N \simeq \lambda_H (\omega_{\text{tr}} - kU - lV) / N, \quad (16)$$

using equation (6). As $-(kU + lV)$ increases (decreases), the intrinsic frequency increases (decreases), and λ_z increases (decreases). Additionally, larger (smaller) λ_z leads to higher (lower) dissipation altitudes (see Figures 4 and 6). We show how thermospheric horizontal winds can alter GW spectra in the next section using a simple convection model.

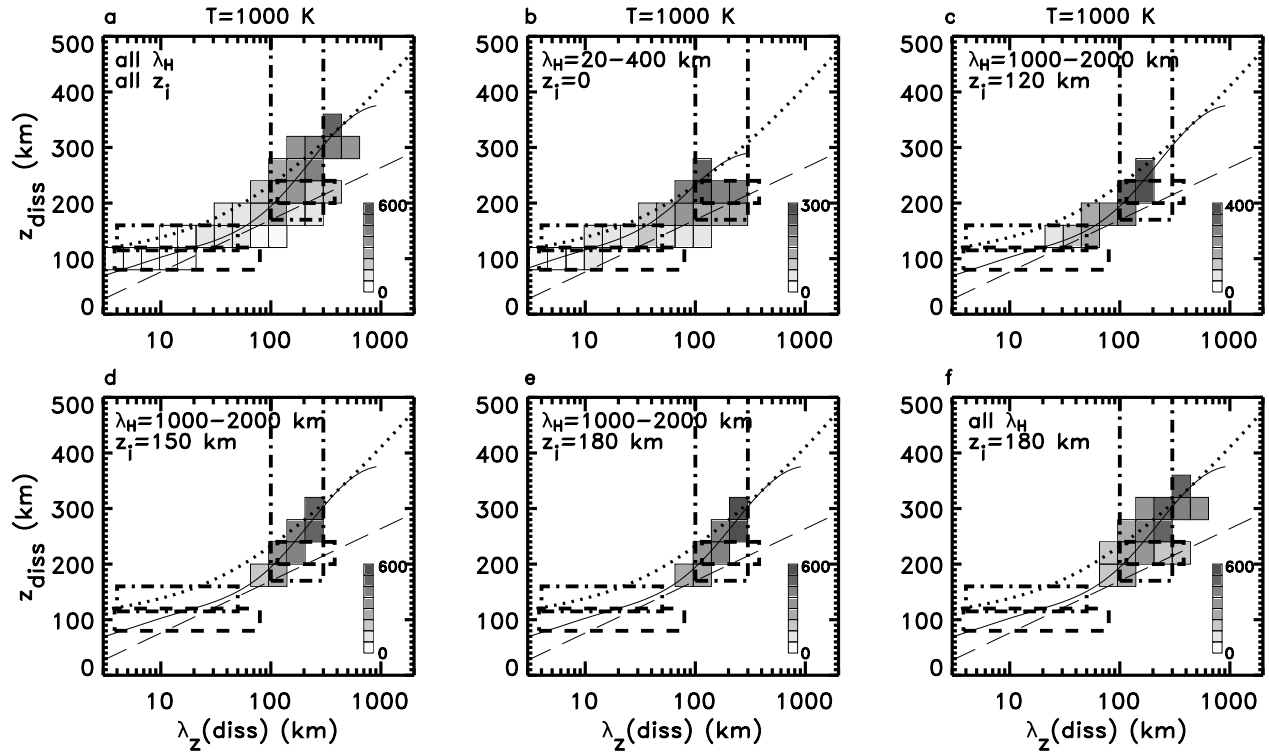


Figure 12. Binned vertical wavelengths at the dissipation altitudes, $\lambda_z(z_{\text{diss}})$, as a function of the binned dissipation altitudes, z_{diss} , for GWs propagating in temperature profile III, as shaded boxes. (a) GWs with $\lambda_H = 20, 50, 100, 200, 300, 400, 1000, 1500,$ and 2000 km launched from $z_i = 0, 120, 150,$ and 180 km. (b) GWs with $\lambda_H = 20, 50, 100, 200, 300,$ and 400 km launched from $z_i = 0$ km. (c) GWs with $\lambda_H = 1000, 1500,$ and 2000 km launched from $z_i = 120$ km. (d) Same as Figure 12c but launched from $z_i = 150$ km. (e) Same as Figure 12c but launched from $z_i = 180$ km. (f) GWs with $\lambda_H = 20, 50, 100, 200, 300, 400, 1000, 1500,$ and 2000 km launched from $z_i = 180$ km. The grey-scale shading of each box shows the average value of $|c_{\text{IH}}|$ for this bin on a linear scale, with a maximum value of 600, 300, 400, 600, 600, and 600 in Figures 12a–12f, respectively.

[42] We also mention another possibility as to why theory and observation can differ when observations infer λ_z from GW phase speeds. Using equation (16), the intrinsic phase speed of a GW is

$$c_{\text{IH}} \sim \lambda_z N / 2\pi. \quad (17)$$

If c_{H} is used in equation (17) instead of c_{IH} because the background winds are not known, then λ_z is calculated to be smaller (larger) than the GW’s real vertical wavelength when the background wind is against (in) the GW’s direction of propagation. In the lower thermosphere, horizontal winds are generally present and vary daily, with speeds up to $100\text{--}200$ m s $^{-1}$. Such large winds can substantially alter the intrinsic properties of observed GWs. As another example, GWs from convection dissipate in the thermosphere in the altitude range, $z \sim 180\text{--}200$, creating body forces and large horizontal winds (VF2006). Because GWs which have not yet dissipated propagate through this region in the same direction as the induced horizontal winds, their intrinsic phase speeds are smaller than they would otherwise be. (GWs propagating in the opposite direction dissipate at lower altitudes). If these induced horizontal winds are neglected, then λ_z is calculated from equation (17) to be larger than the GW’s true vertical wavelength.

[43] Figures 12c, 12d, and 12e shows the theoretical results for only those GWs with $\lambda_H = 1000\text{--}2000$ km launched from $z_i = 120, 150,$ and 180 km, respectively. The agreement with observations at $z = 170\text{--}330$ km is excellent for GWs launched from $z_i \sim 150\text{--}180$ km because GWs with $\lambda_z(z_i) < 100$ km dissipate within $H/2$ of the launch altitude (see Figure 6) and thus are not included here. Because Figure 12e only includes large-scale GWs, and because thermospheric body forcings at $z \sim 180$ km likely generate medium-scale GWs as well (VF2006), we show in Figure 12f the same results as in Figure 12e but for all GWs (small, medium, and large) launched from $z_i = 180$ km. Again, the theoretical predictions agree very well with observations because the small and medium-scale GWs capable of propagating and dissipating away from the launch site have $\lambda_z > 100$ km, consistent with observations.

[44] Finally, we overlay the solid line in Figure 10 (the “fit” line from the work of *Oliver et al.* [1997]) as long dash lines in Figure 12. Although it matches the slope well for GWs with small to medium λ_z , it does not match the slope for GWs with large λ_z when $z > 200$ km. Excellent fits are obtained instead by the curved solid lines, which are the iterative solutions of our dissipation condition, equation (13), using temperature profile III and $\lambda_H = 1500$ km for all except

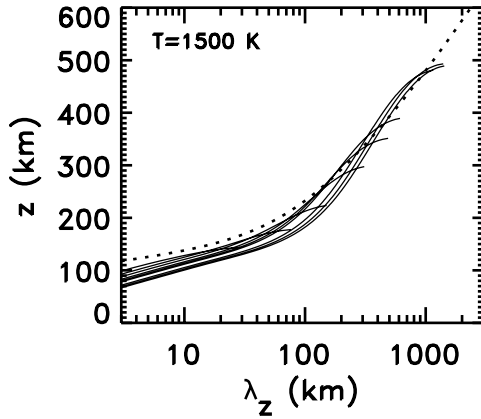


Figure 13. Dissipation condition, equation (13), shown as solid lines using temperature profile IV for GWs with horizontal wavelengths of $\lambda_H = 20, 50, 100, 200, 300, 400, 1000, 1500, 2000$ km. The dot line shows the quenching criteria of *Hines* [1964], equation (18), using the same temperature profile.

Figure 12b where $\lambda_H = 200$ km is used instead. We also overlay the quenching criteria of *Hines* [1964] (dotted line),

$$\lambda_z \simeq 2(3)^{3/4} \pi^{3/2} \nu^{1/2} N^{-1/2}. \quad (18)$$

Hines' quenching criteria underestimates the vertical wavelengths for $z \lesssim 300$ km because *Hines*' derivation is based on the value of λ_z when dissipation just starts to affect a GW and does not take into account the growth of λ_z above that altitude.

[45] Figure 13 shows the iterative solutions of the dissipation condition for GWs with $\lambda_H = 20$ –2000 during active solar conditions. Although each solution is distinct because of the altitudinal “ceiling” which prevents further vertical penetration for GWs with a fixed value of λ_H , the upward trends of the solutions are similar, with only small altitudinal differences. This explains why the $\lambda_H = 1500$ km dissipation condition shown in Figure 12a, for example, is an excellent fit even in the lower thermosphere where small- and medium-scale GWs likely dominate. We see that $\lambda_z(z_{\text{diss}})$ grows exponentially with altitude, although with a smaller slope for $z > 200$ km. We also overlay *Hines*' quenching criteria in Figure 13.

5. Spectral Evolution of GWs in the Thermosphere From Convection

[46] In section 4, we displayed GW dissipation curves with altitude for a wide range of GWs. However, we did not consider how GW spectra from specific sources might evolve with altitude. In particular, GWs may be observed at altitudes lower or higher than z_{diss} if their amplitudes are large enough. Additionally, background winds can alter the observed spectra significantly. In this section, we estimate the evolution of a GW spectrum which is generated from a single, deep plume in a local convection model, as described in the works of *Vadas and Fritts* [2004, 2006]. This plume (plume 8) is created from a vertical body force with full duration 15 min, full diameter $\simeq 18$ km, and full depth $\simeq 12$ km. This yields a convective plume with a

maximum vertical updraft velocity of ~ 6 m s $^{-1}$. The GW momentum flux spectrum in flux content form is shown in Figure 14.

[47] We now estimate how this GW spectrum evolves with altitude in a simple zero-wind environment using the ray-trace results from Figure 4. The spectral filtering is assumed to be kinematic viscosity and thermal diffusivity only; thus we are neglecting the filtering effects from eddy viscosity, ion drag, wave saturation, and wave breaking. Because $u'w'$ and m are only outputted at $z_i, z_{\text{max}}, z_{\text{diss}}$, and $z_{u'w'/2}$ for these runs, some assumptions are needed in order to estimate $\overline{u'w'}$ and m at all altitudes for each GW. Here z_{max} is the altitude below or at z_{diss} where λ_z is maximum and equals $\lambda_z(z_{\text{max}})$.

[48] 1. For $z \leq z_{\text{max}} - H$, $\overline{u'w'}$ is assumed to grow as $\overline{\rho}(z_i)/\overline{\rho}$, and m is calculated from the nondissipative GW anelastic dispersion relation given by equation (6);

[49] 2. For each of the altitude ranges $z_{\text{max}} - H \leq z \leq z_{\text{max}}$, $z_{\text{max}} \leq z \leq z_{\text{diss}}$, and $z_{\text{diss}} \leq z \leq z_{u'w'/2}$, $\overline{u'w'}$ and λ_z are linearly interpolated;

[50] 3. For $z_{u'w'/2} \leq z \leq z_{u'w'/2} + H$, $\overline{u'w'}$ is driven exponentially to 0 using the arbitrarily chosen function $\exp(-5(z - z_{u'w'/2})/H)$. Additionally, λ_z grows linearly with altitude with the same slope if $\lambda_z(z_{u'w'/2}) > \lambda_z(z_{\text{diss}})$; otherwise, λ_z is linearly interpolated to $\lambda_z(z_i)$;

[51] 4. For $z \geq z_{u'w'/2} + H$, $\overline{u'w'} = 0$ and $\lambda_z = \lambda_z(z_{u'w'/2} + H)$.

[52] The GWs in this spectrum have horizontal wavelengths from 10–3020 km in 10-km increments and vertical wavelengths from 5–309 km in 4-km increments and are launched from $z_i = 0$ in the troposphere. We do not include those GWs which violate equations (9) and (10) or have intrinsic periods $\tau_{\text{Ir}} > 6$ hours. We show the resulting vertical wavelength (first row), horizontal wavelength (second row), intrinsic wave period (third row), and intrinsic horizontal phase speed (forth row) spectra as functions of altitude in Figure 15 for thermospheric temperatures 600 K (left column), 1000 K (middle column), and 1500 K (right column). The shaded boxes in Figure 15 show those GWs with amplitudes that are at least 90% of the maximum GW amplitude at that altitude, while the extended rectangular

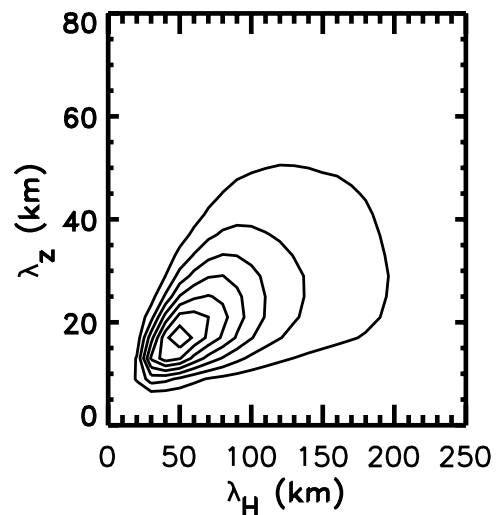


Figure 14. GW momentum flux spectrum in flux content form modeled after a single, deep, convective plume (solid lines). The contours show the amplitudes in intervals of $1/7$ of the maximum value.

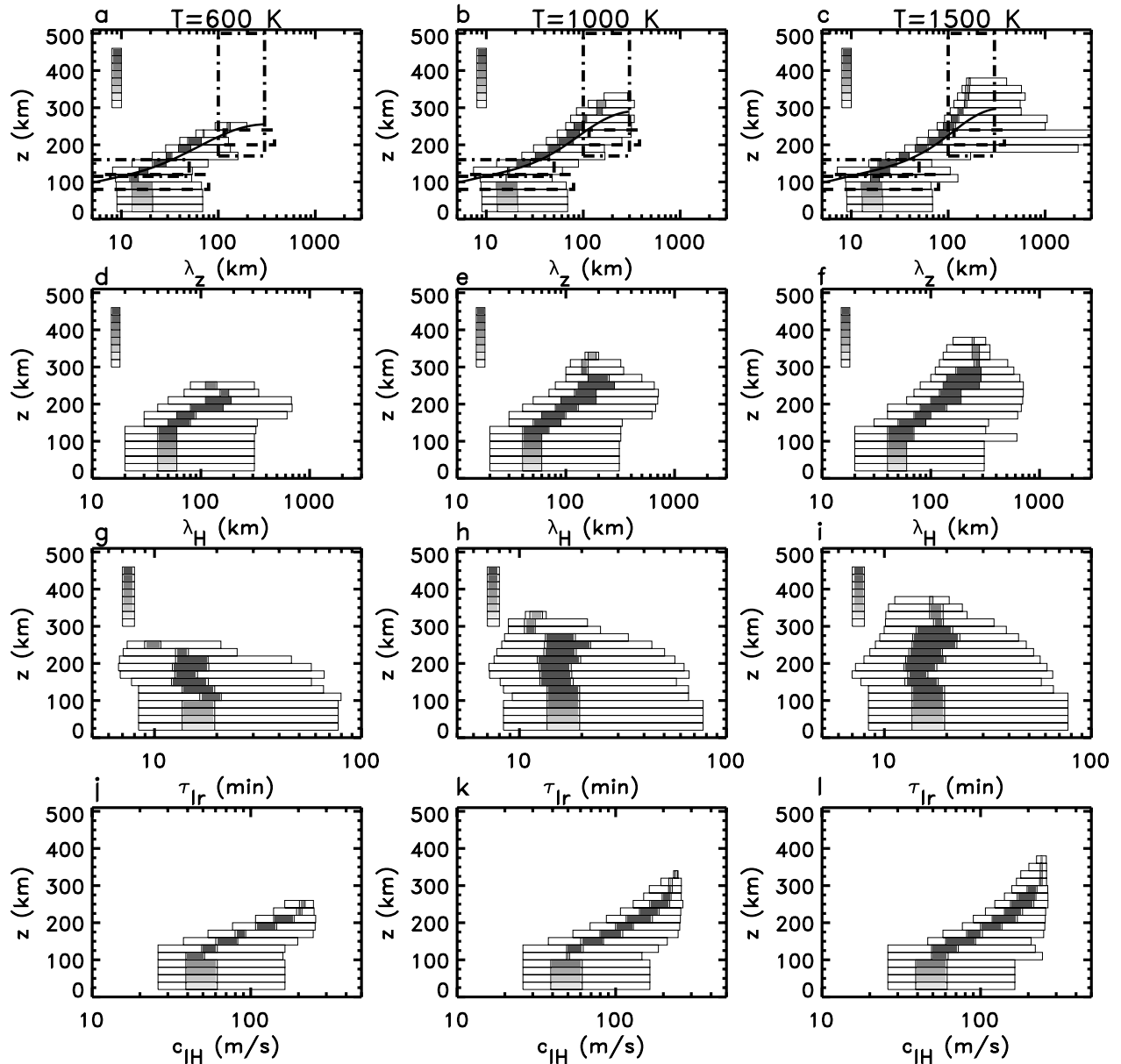


Figure 15. Estimated GW spectra as a function of altitude for the GWs in Figure 14 launched from $z_i = 0$ in temperature profiles II, III, and IV in the left, middle, and right columns, respectively. (a–c) Vertical wavelength spectra. (d–f) Horizontal wavelength spectra. (g–i) Intrinsic wave period spectra. (j–l) Intrinsic horizontal phase speed spectra. The values of the grey-scale shading are described in the text. The light to dark shading indicates the values 0–1.0 in intervals of 0.125, as shown by the color bar in the upper left-hand corner of each plot.

boxes with no shading show those GWs with amplitudes that are at least 25% of the maximum GW amplitude at that altitude. The grey-scale color of the shading indicates the value of $\beta(z) = \log_{10}$ of the maximum momentum flux amplitude at that altitude, divided by the largest value of β for all altitudes. Below $z \sim 125$ km, GWs with amplitudes that are $>90\%$, the maximum have $\lambda_z \lesssim 20$ km, while those GWs with amplitudes that are $>25\%$, the maximum have $\lambda_z \lesssim 70$ km. Similar sensitivities occur in the horizontal wavelength and intrinsic period spectra. Therefore the particular GWs observed at a given altitude depends on the sensitivity of the observations, with more sensitive observa-

tions seeing a proportionately larger portion of the convective GW spectrum.

[53] In Figure 15, λ_z increases exponentially with altitude above $z \sim 125$ km, although with a smaller slope for $z > 200$ km. This is because GWs with initially “undetectable,” small amplitudes are eventually detectable in the thermosphere, since their amplitudes grow exponentially with altitude and those GWs with larger initial amplitudes (but with smaller λ_z) are dissipatively filtered out of the spectrum. The exponential increase also occurs because each GW’s λ_z increases with z as the temperature increases. We also see that λ_H increases rapidly with altitude as well for

$z > 125$ km. The intrinsic periods, however, do not change appreciably with altitude. This is likely because typical GW periods from convection lie in the range of wave periods for GWs which can propagate to the highest altitudes (see Figure 9c). As expected, the GWs with significant amplitudes penetrate to the highest altitudes when the thermosphere is the hottest, $z \sim 225, 300,$ and 325 km in temperature profiles II, III, and IV, respectively. As a function of thermospheric temperature, the largest variations occur in the vertical wavelength spectra; from extreme solar minimum to solar maximum, the peak vertical wavelength of GWs with reasonably significant amplitudes doubles from $\lambda_z \sim 60$ km to $\lambda_z \sim 120$ km. The GWs which penetrate to the highest altitudes of $z \sim 300$ km with amplitudes that are $>25\%$ of the maximum amplitude at that altitude in a $\bar{T} = 1000$ K thermosphere, for example, are medium scale and have $\lambda_z \sim 50\text{--}300$ km, $\lambda_H \sim 100\text{--}300$ km, $\tau_{\text{tr}} \sim 10\text{--}30$ min, and $c_{\text{IH}} \sim 100\text{--}250$ m s $^{-1}$. These large vertical scales, horizontal scales, and intrinsic phase speeds are not characteristic of the dominant convective scales in the initial GW spectrum. In contrast, those GWs at the peak of the initial convective spectrum have $\lambda_z(z_i) \sim 15$ km, $\lambda_H \sim 50$ km, and $c_{\text{IH}} \sim 50$ m s $^{-1}$ and dissipate at $z_{\text{diss}} \sim 130$ km from Figure 4c.

[54] We overlay the dissipation condition, equation (13), for $\lambda_H = 200$ km for each temperature profile as solid lines in Figure 15a–15c. Because the dissipation condition predicts the altitudes at which GWs are dissipating, the actual GW spectra (consisting of dissipating and not-yet-dissipating GWs) are centered at smaller vertical wavelengths for a given altitude, especially at the highest altitudes. We also overlay the observational results of *Oliver et al.* [1997] and *Djuth et al.* [1997, 2004] as dash and dash-dot boxes, respectively. The observational results agree very well with this model spectrum for $z = 80\text{--}170$ km. For $z = 170\text{--}250$ km, however, many of these GWs do not have large enough λ_z to agree with these observations.

[55] Although GWs from convection in a zero-wind environment do not appear to have large enough λ_z at $z \simeq 170\text{--}250$ km to agree with observations, strong background winds can substantially lengthen GW vertical wavelengths to better agree with observations. Here we consider the same convective GW spectrum shown in Figure 14 but with a sudden westward wind of $U = -100$ m s $^{-1}$ above $z \geq 120$. Using equations (6) and (12), we recalculate the vertical wavelengths of GWs at $z = 120$ km that have $z_{\text{max}} - H > 120$ km (i.e., that are not yet dissipating). Then we use the $z_i = 120$ km launch solutions with the closest values of $\lambda_z(z_i)$ in order to determine the values of $\overline{u'w'}$ and m at the new values of z_{max} , z_{diss} , and $z_{\overline{u'w'}/2}$. Finally, we use the same approximate altitude ranges as before to estimate $\overline{u'w'}$ and m as a function of altitude above $z \geq 120$ km. The initial GW spectrum is approximated to be $2D$, and we assume that it contains equal amounts of eastward and westward-propagating GWs.

[56] In Figure 16, we show the estimated vertical and horizontal wavelength, ground-based wave period, and ground-based horizontal phase speed spectra for GWs propagating in temperature profile III. The boxes and shading are the same as in Figure 15, with the shaded (unshaded) rectangular boxes showing the GWs with amplitudes that are 90% (25%) of the maximum amplitude at that altitude. Additionally, Figure 16a shows the dissipation condition

with $\lambda_H = 200$ km (solid line) and the same Oliver and Djuth results shown in Figure 15a–15c. We see that the vertical wavelengths of GWs for $z > 170$ km are much larger here than in the zero-wind example because of the Doppler shifting of the eastward-moving GWs; in particular, there are no longer GWs with $\lambda_z \sim 20\text{--}100$ km in the $z \simeq 170\text{--}250$ km altitude range. However, the horizontal wavelengths, ground-based periods, and horizontal phase speeds for the GWs reaching the highest altitudes of $z \sim 325$ km (with significant amplitudes) at the 25% detection level are not very different from when there are no thermospheric winds, $\lambda_H \simeq 100\text{--}300$ km, $\tau_{\text{tr}} \sim 10\text{--}40$ min, and $c_{\text{IH}} \sim 100\text{--}250$ m s $^{-1}$. The GW spectra at the highest altitudes are composed nearly entirely of eastward-propagating GWs in this example; those GWs propagating in the direction of the wind negligibly affect the spectra because they dissipate at lower altitudes where their amplitudes are smaller. Additionally, GWs moving perpendicular to the background wind (northward and southward in this example) would also negligibly affect the spectra if included because their vertical wavelengths would not change from the wind, so they would dissipate at lower altitudes with smaller amplitudes as well (VF2006).

[57] Figure 16a shows that the Doppler-shifted thermospheric GW spectrum agrees very well with observations for $z \geq 170$ km. The result that modeled GW spectra from convection agree well with observations for $z \geq 170$ km when strong thermospheric winds are present (and does not agree well for zero background winds) should not be surprising, as horizontal winds in the thermosphere tend to be strong because of diurnal and semidiurnal tides, with magnitudes of order $\sim 100\text{--}200$ m s $^{-1}$ [e.g., *Roble and Ridley*, 1994; *Larsen*, 2002; *Larsen et al.*, 2003]. Therefore it is likely in general that lower atmospheric GW spectra are Doppler-shifted to larger λ_z in the direction opposite to prevailing background winds in the thermosphere. We emphasize that this model GW spectrum is a simple example that we assumed in order to gain a better understanding of the relationship between observed GW scales and theoretical predictions using this new anelastic dispersion relation. Further work using ray tracing with realistic temporally and spatially variable GW convective spectra and realistic background winds are needed for better comparison with observations.

6. Conclusions

[58] In this paper, we explored many properties of a new anelastic, GW dispersion relation which includes kinematic viscosity and thermal diffusivity in the thermosphere. We calculated the dissipation altitudes, range of vertical wavelengths, horizontal distances traveled, and time taken for GWs to travel until they dissipate for GWs with horizontal wavelengths of $10\text{--}3020$ km and vertical wavelengths of $5\text{--}400$ km, for four different temperature profiles from extreme solar minimum to very active solar conditions and for four different launch altitudes in the lower atmosphere and thermosphere. These results were shown and described in Figures 4–7. Because of the complexity of the results and because the dissipation altitudes and maximum vertical wavelengths only depend on the intrinsic wave properties, our calculations did not include background winds. However, we explained how background winds can be included

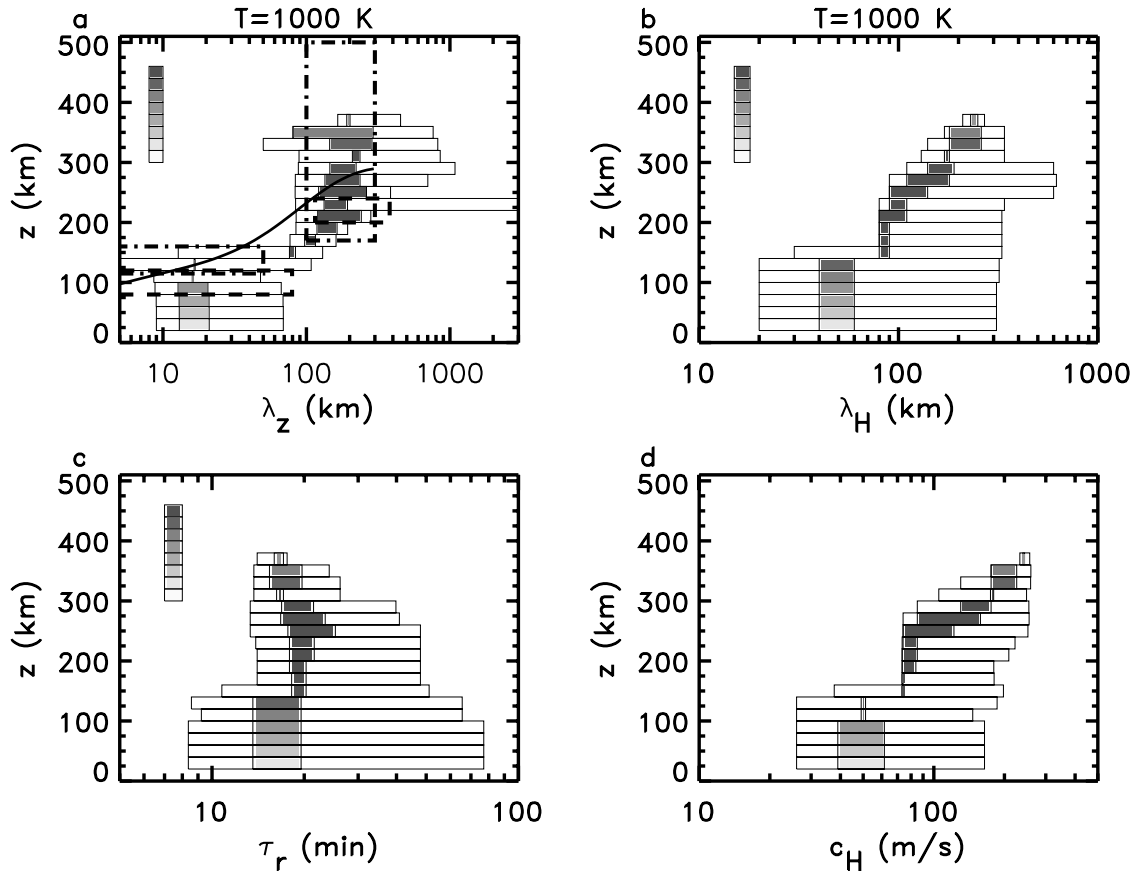


Figure 16. Estimated GW spectra as a function of altitude for convective GWs launched from $z_i = 0$ in temperature profile III. A sudden shear of -100 m s^{-1} is assumed at $z = 120 \text{ km}$. (a) Vertical wavelength spectrum. (b) Horizontal wavelength spectrum. (c) Ground-based wave period spectrum, τ_r . (d) Ground-based horizontal phase speed spectrum, c_H . The shading is the same as in Figure 15.

to obtain GW dissipation altitudes and maximum vertical wavelengths when background winds are known. Therefore Figures 4–7 can be used as look-up figures if the approximate intrinsic GW properties at or near the dissipation altitudes are known or can be estimated. Note that the dissipation altitude, z_{diss} is defined as the altitude where a GW’s momentum flux is maximum and is therefore not the maximum altitude attainable by a GW. Instead, we showed that GWs can be observed one to two density scale heights above z_{diss} . We also found that GWs generated in the thermosphere with large enough horizontal phase speeds will appear quasiperiodic because they typically only oscillate through one-half to two wave cycles before dissipating, depending on the launch altitude and thermospheric temperature.

[59] For GWs with the same horizontal wavelength λ_H , we found that λ_z at z_{diss} (i.e., $\lambda_z(z_{\text{diss}})$) increases approximately linearly with altitude because of the increase of the initial vertical wavelengths $\lambda_z(z_i)$ in the GW spectra. However, if a GW’s intrinsic frequency nears the thermospheric buoyancy frequency, then $\lambda_z(z_{\text{diss}})$ increases much more rapidly with z_{diss} . We combined our ray-trace results for GWs with differing λ_H and $\lambda_z(z_i)$ and found that as a whole, $\lambda_z(z_{\text{diss}})$ increases exponentially with z_{diss} , although with a smaller slope for $z > 200 \text{ km}$. These results agree well with observational data of *Oliver et al.* [1997] and *Djuth et al.* [1997, 2004]. We found that GWs dissipating at the highest

altitudes of $z \sim 400\text{--}500 \text{ km}$ have horizontal scales $\lambda_H \simeq 400\text{--}2000 \text{ km}$ and intrinsic wave periods of $\tau_{\text{Ir}} \simeq 10\text{--}50 \text{ min}$. Additionally, GWs with $\lambda_H \leq 20 \text{ km}$ (commonly observed in airglow images near the mesopause) do not dissipate above $z \sim 150 \text{ km}$, and GWs with $\tau_{\text{Ir}} \leq 7 \text{ min}$ and $\tau_{\text{Ir}} \geq 300 \text{ min}$ do not dissipate above $z \sim 150 \text{ km}$ as well. We also found that our dissipation condition, which calculates the estimated vertical wavelengths of dissipating GWs as a function of altitude [given by equation (13)], agrees with the ray trace results very well (solid lines in Figures 8, 12, 13, 15, and 16).

[60] Last, we employed a simple GW spectrum modeled after a deep plume in tropospheric convection to estimate the horizontal wavelength, vertical wavelength, and wave period spectra with altitude. We found that dissipative filtering caused the GW spectra to shift to increasingly larger horizontal and vertical scales while propagating upwards in the thermosphere, with differing portions of the initial GW spectra being important at differing altitudes within the thermosphere. The wave period spectrum, however, did not alter appreciably with altitude. This is likely because typical GW periods from convection lie in the range of wave periods for GWs which can propagate to the highest altitudes. At altitudes above $z \sim 135 \text{ km}$, the horizontal and vertical scales which dominate the GW spectra are not characteristic of the typical scales in the initial convective

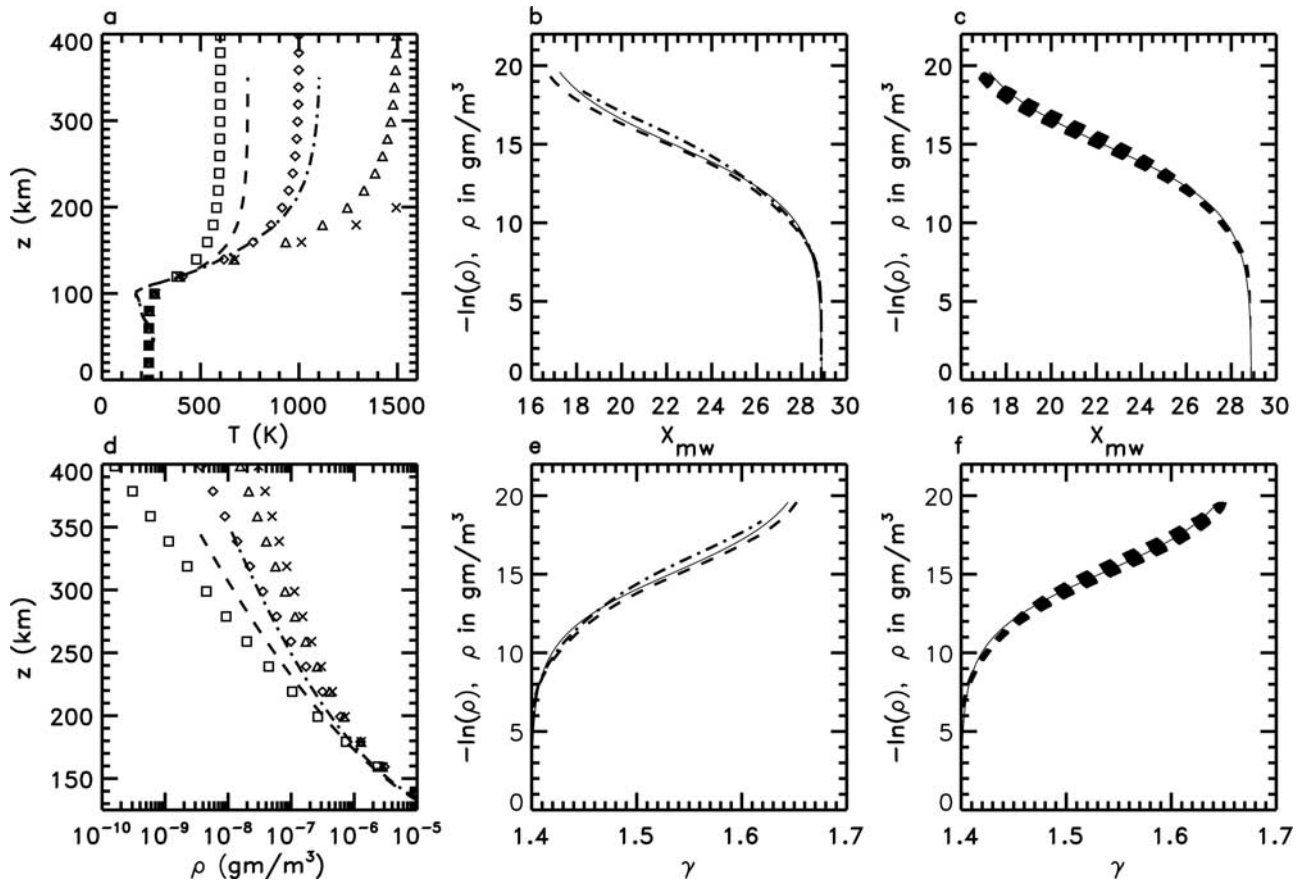


Figure A1. (a) Minimum and maximum TIME-GCM temperature profiles (dash and dash-dot lines, respectively). Boxes, diamonds, triangles, and Xs show our temperature profiles II, III, IV, and V, respectively. (b) Mean molecular weight profiles, X_{MW} , for the minimum and maximum TIME-GCM thermospheric temperature profiles shown in Figure A1a as dash and dash-dot lines, respectively. The solid line shows the “best fit” distribution given by equation (3). (c) Mean molecular weight profiles, X_{MW} , for all TIME-GCM model data (dash lines). Solid line same as in Figure A1b. (d) Same as in Figure A1a but showing the density profiles. (e) Ratio of mean specific heat capacities, γ , for the minimum and maximum TIME-GCM thermospheric temperature profiles shown in Figure A1a as dash and dash-dot lines, respectively. The solid line shows the “best fit” distribution given by equation (4). (f) Profiles of mean γ for all TIME-GCM model data (dash lines). Solid line same as in Figure A1e.

GW spectrum. This may be one of the reasons it has been difficult to trace GWs in the thermosphere back to specific small-scale tropospheric convective regions. The GWs with the largest amplitudes which penetrate to the highest altitudes of $z \sim 300$ km in a $\bar{T} = 1000$ K thermosphere, for example, have $\lambda_z \sim 100$ km, $\lambda_H \sim 100\text{--}300$ km, intrinsic wave periods of $\tau_{Ir} \simeq 10\text{--}20$ min, and intrinsic horizontal phase speeds of $c_{IH} \sim 200$ m s⁻¹. We also estimated the GW spectra in the thermosphere for GWs excited from the same convective plume but which propagated through a shear of -100 m s⁻¹ in the lower thermosphere. We found that the vertical wavelength spectra shifted to much larger $\lambda_z \sim 100\text{--}300$ km for $z \geq 170$ km, thereby agreeing well with observational results in this altitude range. We also found that those GWs penetrating to the highest altitudes have horizontal wavelengths and ground-based phase speeds that are similar to those when background winds are zero. Because convection may generate medium-scale GWs in the F region with horizontal phase speeds of $c_H \sim 100\text{--}250$ m s⁻¹, because medium-scale TIDs with these character-

istics are ubiquitous in the ionosphere, and because our results show that these GWs may travel up to 2000 km horizontally from their source prior to dissipating, our results suggest that some of these observed TIDs may be a direct result of convection.

Appendix A: Molecular Weight and Ratio of Specific Heat Capacities

[61] The TIME-GCM model data used to calculate the “best fit” functions for X_{MW} and γ as a function of the mean density used in this paper encompass 28 September 2004 to 27 October 2004 over Brazil, with latitudes of -22.5° to -2.5° and longitudes of -60° to -40° on a 5° grid. The TIME-GCM is a global mesospheric and thermospheric dynamics and chemistry model [e.g., *Roble and Ridley, 1994*]. Our analysis only utilized the model data every 3 hours. During this period, the minimum and maximum thermospheric temperatures were 740 and 1100 K, respectively. We show these temperature profiles in Figure A1a

along with the temperature profiles we use in this paper. Our temperatures are consistent with the TIME-GCM temperatures in the lower thermosphere above the cold mesopause. Figure A1b shows the mean X_{MW} for these minimum and maximum TIME-GCM temperature profiles, along with our “best fit” profile [equation (3)]. Figure A1c shows the best fit profile as well as all of the mean X_{MW} profiles for this month. The best fit analytic function for X_{MW} fits the model data very well. Figure A1d shows the mean density profiles for the minimum and maximum TIME-GCM temperature profiles shown in Figure A1a, as well as the density profiles we use in this paper. Our densities are consistent with the TIME-GCM mean densities in the lower thermosphere (at $z \sim 125$ km). Figure A1e shows the ratio of the mean C_p to mean C_v profiles for the minimum and maximum TIME-GCM temperature profiles shown in Figure A1a, along with our “best fit” profile [equation (4)]. Figure A1f shows the best fit profile as well as all of the mean γ profiles for this month. Again, the best fit analytic function for γ fits the TIME-GCM model data very well.

[62] **Acknowledgments.** This research was supported by the National Science Foundation under grants ATM-0307910 and ATM-0537311. The author would like to thank Ray Roble and Han-Li Liu for the TIME-GCM data and Frank Djuth for helpful comments regarding this manuscript.

[63] Zuyin Pu thanks Michael Hickey and Frank Djuth for their assistance in evaluating this paper.

References

- Banks, P. M., and G. Kockarts (1973), *Aeronomy Part A*, 430 pp., Elsevier, New York.
- Bauer, S. J. (1958), An apparent ionospheric response to the passage of hurricanes, *J. Geophys. Res.*, **63**, 265–269.
- Bishop, R., N. Aponte, G. D. Earle, M. Sulzer, M. F. Larsen, and G. Peng (2006), Arecibo observations of ionospheric perturbations associated with the passage of tropical storm Odette, *J. Geophys. Res.*, **111**, A11320, doi:10.1029/2006JA011668.
- Bristow, W. A., and R. A. Greenwald (1996), Multiradar observations of medium-scale acoustic gravity waves using the Super Dual Auroral Radar Network, *J. Geophys. Res.*, **101**, 24,499–24,511.
- Bristow, W. A., R. A. Greenwald, and J. C. Samson (1994), Identification of high-latitude acoustic gravity wave sources using the Goose Bay HF radar, *J. Geophys. Res.*, **99**, 319–331.
- Bristow, W. A., R. A. Greenwald, and J. P. Villain (1996), On the seasonal dependence of medium-scale atmospheric gravity waves in the upper atmosphere at high latitudes, *J. Geophys. Res.*, **101**, 15,685–15,699.
- Cole, K. D., and M. P. Hickey (1981), Energy transfer by gravity wave dissipation, *Adv. Space Res.*, **1**, 65–74.
- Crowley, G., T. B. Jones, and J. R. Dudeney (1987), Comparison of short period TID morphologies in Antarctica during geomagnetically quiet and active intervals, *J. Atmos. Terr. Phys.*, **49**, 1155–1162.
- Dalgarno, A., and F. J. Smith (1962), *Planet. Space Sci.*, **9**, 1.
- Del Genio, A. D., and G. Schubert (1979), Gravity wave propagation in a diffusively separated atmosphere with height-dependent collision frequencies, *J. Geophys. Res.*, **84**, 4371–4378.
- Dewan, E. M., R. H. Picard, R. R. O’Neil, H. A. Gardiner, J. Gibson, J. D. Mill, E. Richards, M. Kendra, and W. O. Gallery (1998), MSX satellite observations of thunderstorm-generated gravity waves in mid-wave infrared images of the upper stratosphere, *Geophys. Res. Lett.*, **25**, 939–942.
- Djuth, F. T., M. P. Sulzer, J. H. Elder, and V. B. Wickwar (1997), High-resolution studies of atmosphere-ionosphere coupling at Arecibo Observatory, Puerto Rico, *Radio Sci.*, **32**, 2321–2344.
- Djuth, F. T., M. P. Sulzer, S. A. Gonzales, J. D. Mathews, J. H. Elder, and R. L. Walterscheid (2004), A continuum of gravity waves in the Arecibo thermosphere?, *Geophys. Res. Lett.*, **31**, L16801, doi:10.1029/2003GL019376.
- Einaudi, F., and C. O. Hines (1970), WKB approximation in application to acoustic-gravity waves, *Can. J. Phys.*, **48**, 1458–1471.
- Francis, S. H. (1973), Acoustic-gravity modes and large-scale traveling ionospheric disturbances of a realistic, dissipative atmosphere, *J. Geophys. Res.*, **78**, 2278–2301.
- Georges, T. M. (1968), HF doppler studies of traveling ionospheric disturbances, *J. Atmos. Terr. Phys.*, **30**, 735–746.
- Gossard, E. E., and W. H. Hooke (1975), *Waves in the Atmosphere*, 112 pp., Elsevier, New York.
- Hickey, M. P., and K. D. Cole (1987), A quartic dispersion equation for internal gravity waves in the thermosphere, *J. Atmos. Terr. Phys.*, **49**, 889–899.
- Hickey, M. P., and K. D. Cole (1988), A numerical model for gravity wave dissipation in the thermosphere, *J. Atmos. Terr. Phys.*, **50**, 689–697.
- Hines, C. O. (1960), Internal atmospheric gravity waves at ionospheric heights, *Can. J. Phys.*, **38**, 1441–1481.
- Hines, C. O. (1964), Minimum vertical scale sizes in the wind structure above 100 kilometers, *J. Geophys. Res.*, **69**, 2847–2848.
- Hines, C. O. (1967), On the nature of travelling ionospheric disturbances launched by low-altitude nuclear explosions, *J. Geophys. Res.*, **72**, 1877–1882.
- Hines, C. O., and W. H. Hooke (1970), Discussion of ionization effects on the propagation of acoustic-gravity waves in the ionosphere, *J. Geophys. Res.*, **75**, 2563–2568.
- Hocke, K., K. Schlegel, and G. Kirchengast (1996), Phases and amplitudes of TIDs in the high-latitude F-region observed by EISCAT, *J. Atmos. Terr. Phys.*, **58**, 245–255.
- Hocke, K., and K. Schlegel (1996), A review of atmospheric gravity waves and traveling ionospheric disturbances: 1982–1995, *Ann. Geophys.*, **14**, 917–940.
- Hocke, K., and T. Tsuda (2001), Gravity waves and ionospheric irregularities over tropical convection zones observed by GPS/MET radio occultation, *Geophys. Res. Lett.*, **28**, 2815–2818.
- Hung, R. J., and J. P. Kuo (1978), Ionospheric observation of gravity-waves associated with hurricane Eloise, *J. Geophys.*, **45**, 67–80.
- Hung, R. J., and R. E. Smith (1978), Ray tracing of gravity waves as a possible warning system for tornadic storms and hurricanes, *J. Appl. Meteorol.*, **17**, 3–11.
- Hung, R. J., T. Phan, and R. E. Smith (1978), Observations of gravity waves during the extreme tornado outbreak of 3 April 1974, *J. Atmos. Terr. Phys.*, **40**, 831–843.
- Klostermeyer, J. (1972), Numerical calculation of gravity wave propagation in a realistic thermosphere, *J. Atmos. Terr. Phys.*, **34**, 765–774.
- Kundu, P. (1990), *Fluid Dynamics*, 638 pp., Elsevier, New York.
- Larsen, M. F. (2002), Winds and shears in the mesosphere and lower thermosphere: Results from four decades of chemical release wind measurements, *J. Geophys. Res.*, **107**(A8), 1216, doi:10.1029/2001JA000218.
- Larsen, M. F., A. Z. Liu, R. L. Bishop, and J. H. Hecht (2003), TOMEX: A comparison of lidar and sounding rocket chemical tracer wind measurements, *Geophys. Res. Lett.*, **30**(7), 1375, doi:10.1029/2002GL015678.
- Lighthill, J. (1978), *Waves in Fluids*, Cambridge Univ. Press, New York.
- Marks, C. J., and S. D. Eckermann (1995), A three-dimensional nonhydrostatic ray-tracing model for gravity waves: Formulation and preliminary results for the middle atmosphere, *J. Atmos. Sci.*, **52**, 1959–1984.
- Midgley, J. E., and H. B. Liemohn (1966), Gravity waves in a realistic atmosphere, *J. Geophys. Res.*, **71**, 3729–3748.
- Ogawa, T., K. Igarashi, K. Aikyo, and H. Maeno (1987), NNSS Satellite observations of medium-scale traveling ionospheric disturbances at southern high-latitudes, *J. Geomagn. Geoelectr.*, **39**, 709–721.
- Oliver, W. L., Y. Otsuka, M. Sato, T. Takami, and S. Fukao (1997), A climatology of F region gravity wave propagation over the middle and upper atmosphere radar, *J. Geophys. Res.*, **102**, 14,499–14,512.
- Pitteway, M. L. V., and C. O. Hines (1963), The viscous damping of atmospheric gravity waves, *Can. J. Phys.*, **41**, 1935–1948.
- Richmond, A. D. (1978), Gravity wave generation, propagation, and dissipation in the thermosphere, *J. Geophys. Res.*, **83**, 4131–4145.
- Roble, R. G., and E. C. Ridley (1994), A thermosphere-ionosphere-mesosphere-electrodynamics general circulation model (TIME-GCM): Equinox solar cycle minimum simulations (30–500 km), *Geophys. Res. Lett.*, **21**, 417–420.
- Röttger, J. (1977), Atmospheric gravity waves generated by penetrative cumulus convection in the tropics, 11th Technical conference on hurricanes and tropical meteorology, AMS, Dec 13–16, Florida.
- Samson, J. C., R. A. Greenwald, J. M. Ruohoniemi, and K. B. Baker (1989), High-frequency radar observations of atmospheric gravity waves in the high-latitude ionosphere, *Geophys. Res. Lett.*, **16**, 875–878.
- Samson, J. C., R. A. Greenwald, J. M. Ruohoniemi, A. Frey, and K. B. Baker (1990), Goose Bay Radar observations of Earth-reflected atmospheric gravity waves in the high-latitude ionosphere, *J. Geophys. Res.*, **95**, 7693–7709.
- Sentman, D. D., E. M. Wescott, R. H. Picard, J. R. Winick, H. C. Stenbaek-Nielsen, E. M. Dewan, D. R. Moudry, F. T. Sao Sabbas, M. J. Heavner, and J. Morrill (2003), Simultaneous observations of mesospheric gravity waves and sprites generated by a midwestern thunderstorm, *J. Atmos. Sol.-Terr. Phys.*, **65**, 5.

- Shiokawa, K., Y. Otsuka, and T. Ogawa (2006), Quasi-periodic southward-moving waves in 630-nm airglow images in the equatorial thermosphere, *J. Geophys. Res.*, *111*, A06301, doi:10.1029/2005JA011406.
- Taylor, M. J., and M. A. Hapgood (1988), Identification of a thunderstorm as a source of short period gravity waves in the upper atmospheric night-glow emissions, *Planet. Space Sci.*, *36*, 975–985.
- Vadas, S. L., and D. C. Fritts (2004), Thermospheric responses to gravity waves arising from mesoscale convective complexes, *J. Atmos. Sol.-Terr. Phys.*, *66*, 781–804.
- Vadas, S. L., and D. C. Fritts (2005), Thermospheric responses to gravity waves: Influences of increasing viscosity and thermal diffusivity, *J. Geophys. Res.*, *110*, D15103, doi:10.1029/2004JD005574.
- Vadas, S. L., and D. C. Fritts (2006), Influence of solar variability on gravity wave structure and dissipation in the thermosphere from tropospheric convection, *J. Geophys. Res.*, *111*, A10S12, doi:10.1029/2005JA011510.
- Volland, H. (1969), Full wave calculations of gravity wave propagation through the thermosphere, *J. Geophys. Res.*, *74*, 1786–1795.
- Waldock, J. A., and T. B. Jones (1986), HF doppler observations of medium-scale travelling ionospheric disturbances at mid-latitudes, *J. Atmos. Terr. Phys.*, *48*, 245–260.
- Waldock, J. A., and T. B. Jones (1987), Source regions of medium scale travelling ionospheric disturbances observed at mid-latitudes, *J. Atmos. Terr. Phys.*, *49*, 105–114.
- Walker, G. O., Y. W. Wong, H. K. Ma, T. Kikuchi, K. Nozaki, Y. N. Hung, and V. Badillo (1988), Propagating ionospheric waves observed throughout east Asia during the WAGS October 1985 campaign, *Radio Sci.*, *23*, 867–878.
- Yanowitch, M. (1967), Effect of viscosity on gravity waves and the upper boundary condition, *J. Fluid Mech.*, *29*, 209–231.
- Yeh, K. C., C. H. Liu, and M. Y. Youakim (1975), Attenuation of internal gravity waves in model atmospheres, *Ann. Geophys.*, *31*, 321–328.
- Zhang, S. D., and F. Yi (2002), A numerical study of propagation characteristics of gravity wave packets propagating in a dissipative atmosphere, *J. Geophys. Res.*, *107*(CD14), 4222, doi:10.1029/2001JD000864.

S. L. Vadas, Colorado Research Associates, NorthWest Research Associates, 3380 Mitchell Lane, Boulder, CO 80301, USA. (vasha@cora.nwra.com)